ORIGINAL ARTICLE

Journal Section

Drift-flux model for gas-liquid flow subjected to centrifugal fields

Penteado, Marcos R. M.[1] | Vieira, S. C.[2] | Castro, Marcelo S. de[1] | Bannwart, A. C.[1]

[1]School of Mechanical Engineering, University of Campinas - UNICAMP - Rua Mendeleyev, 200 - Campinas SP - CEP: 13083-970, Brazil

[2]Petrobras S.A. - Av. Republica do Chile, 65 - Rio de Janeiro RJ - CEP: 20031-912, Brazil

Correspondence
Penteado, Marcos R. M.
Email: mendesmarkitto@gmail.com

Funding information
Petróleo Brasileiro S.A - Petrobras and PRH-ANP - Agência Nacional do Petróleo

Centrifugal pumps are used in several industrial processes. It is common the operation of this equipment with gas-liquid mixtures, which is the case of the electrical submersible pumping artificial lift method used in the oil industry. The increase of free gas fraction inside the pump may lead to unstable operation and problems such as surging and gas locking phenomena to occur. In this study a drift-flux model is proposed for the gas-liquid flow subjected to centrifugal fields using the impeller as an example. The model is closed with experimental data of bubble diameter, displacements and velocities acquired via high-speed camera at several different rotational speeds and gas mass flow rates using water as the continuous medium. From the modeling and the forces balance in the bubbles, a quantitative criterion for the start point of surging and gas locking conditions was proposed.

KEYWORDS

Electric submersible pump; Two-phase flow; Gas-liquid flows; Drift-flux model; Bubbles characteristics.

*Equally contributing authors.

Nomenclature

Lattin Letters

B_b	-	Bubble volume	I	-	Impeller rotation between frames
C_B	-	Basset coefficient	M	-	Momentum transfer
C_D	-	Drag coefficient	$\dot{m}$	-	Mass flow rate
C_V	-	Virtual mass coefficient for bubbles	P	-	Pressure
d	-	Diameter	ΔP	-	Pump pressure increment
$\vec{F}$	-	Sum of the forces	Q_{BEP}	-	Liquid flow rates at the best efficiency point
$\vec{F}_B$	-	Basset force	Q	-	Flow rate
$\vec{F}_D$	-	Drag force	Q^*	-	Dimensionless flow rate
$\vec{F}_P$	-	Pressure force	r_i	-	Impeller channel intake radius
$\vec{F}_V$	-	Added mass force	r_o	-	Impeller channel exit radius
$\vec{g}$	-	Gravitational acceleration	r_b	-	Bubble radius
H	-	Head	$\vec{V}$	-	Velocity vector in absolute frame of reference
H^*	-	Dimensionless head	$\vec{v}$	-	Relative velocity vector

Greek Letters

α	-	Gas void fraction	τ	-	Stress tensor
β	-	Blade angle	μ	-	Viscosity
θ	-	Tangential coordinate	Ω	-	Rotational vector
ρ	-	Density	ω	-	Angular velocity
σ	-	Interfacial or surface tension	$\Delta\rho$	-	Density difference between phases

Subscripts

1	-	Liquid/water phase	o	-	Exit
2	-	Gas/air phase	r, θ	-	Polar coordinate system components
b	-	Bubble	s, n	-	Blade coordinate system components
m	-	Mixture	BEP	-	Best efficiency point
i	-	Intake			

1 | INTRODUCTION

Electric Submersible Pump (ESP) is an artificial lift method used in the petroleum industry. The objective is to increase the energy present in the fluid inside the reservoir and bring it to the surface. The internal flow is extremely complex, involving turbulence effects, system rotation, separation and streamline curvature suffering influence of convex and concave walls. Moreover, the flow is influenced by interaction mechanisms or other unsteady effects because of the presence of a mobile structure and a static structure: impeller and diffuser (Feng et al., 2010 [1]).

In the past few decades, many experimental studies and modeling approaches have been made by many researches to predict ESP pressure increment under gas-liquid flow conditions. Some analytical models are available in the literature for predicting head degradation from low to high void fractions for the nuclear industry, such as Mikielewicz et al. (1978) [2] and Wilson et al. (1979) [3]. These models used a semi-empirical approach, obtaining correlations from single-phase and two-phase flows from experimental data. Some works related to these flows in pumps are Estevam (2002) [4], Barrios (2007) [5], Solano (2009) [6], Paternost (2013) [7], Biazussi (2014) [8], among others.

The acquisition of flow characteristics inside the pump is not an easy job due to the high pressures that these equipment are submitted. The improvements in the pump operation can bring considerable benefits for the industry. Some approaches related to visualization studies were conducted to observe multiphase flow structures, such as the

flow patterns inside a rotating centrifugal pump. Some studies may be cited in this case which are: Murakami and Minemura (1974) [9]-[10], Estevam (2002) [4], Gamboa (2009) [11], Monte Verde et al. (2017) [12] and others. Most of these studies used transparent casing to visually observe the pump internal flow patterns. Starting with the original volute-type centrifugal pumps, they cover several research topics, such as flow pattern recognition, bubble movement visualization, mapping transition boundaries etc.

Estevam (2002) [4] conducted the first study on flow patterns inside ESP. His study emphasizes the ESP performance under certain conditions considering the influence of the amount of air bubbles, which leads to surging and gas locking. The pump of his experiment had two stages and was under a stratified and dispersed bubble flow, with the following variables acquired: void fraction between 0 to 15% at the entrance of the pump, liquid and gas flow rates, inlet and outlet pressure, pump rotation and pump axis torque. The author identified a dimensionless number as a surging indicator, I_S, after applying the two-fluid model. This number relates the drag and centrifugal force with void fraction at the inlet of the impeller, being an important indicator for the pump performance.

Barrios (2007) [5] developed a model based on bubble diameter to determine surging conditions. The author proposed an approach based on a mechanistic model, considering one-dimensional based on the balance of forces acting on bubbles, which are: centrifugal, drag and pressure. This model depends on two important variables. The first is the bubble diameter which may cause its own stagnation in the impeller channels and the second is the drag coefficient. The model assumes that for a bubble diameter lower than a critical one, the drag force pushes them into the diffuser. Larger bubbles remained stationary at admission and coalesced with new bubbles that had the same diameter, accumulating, which causes coalescence and then surging. In some cases, this model showed a good agreement with the experimental data.

The actual head developed by the pump is always less than theoretical one. Vieira (2014) [13] performed a simulation in order to study the pump losses. The velocity fields showed the presence of vortex in the channels of the impeller at partial flow rates (outside the Best Efficiency Point - BEP), with more intensity for the less viscous case. At the BEP the vortex were despicable or absent. The largest discrepancies in the numeric simulation were observed at flow rates distancing from BEP and in lowest flow rates, particularly with pump working with water. Another discrepancy concluded by its works refers to the friction factor. Comparing this variable for water, the experimental values were higher than those calculated by the simulations, specially for high flow rates. However, for viscous fluids, the friction factor was the opposed, their values were less than those given by the numerical simulations. In her study, the losses were treated numerically, an alternative tool to understand better the phenomena inside the ESP.

Biazussi (2014) [8] performed an experimental study to get the ESP performance operating with two-phase gas-liquid flows. Three pump models were tested, P23, P47 and P100, all of them having three stages. The study comprised the analyses of three main characteristics, which could be related to pump performance, namely: rotational velocity, which ranged between 1800 and 3500 rpm; suction pressure varying between 100 and 500 kPa; and gas mass flow rate, kept constant in the experiments. The author concluded that changes in pump rotation affects pump performance and transition patterns. Increasing the velocity of the impeller also increases the centripetal force acting on the bubble. The flow rate rises along with it. Thus, two forces are raising together in this situation, the buoyancy force proportioned by the increase of the flow rate and the centripetal force raised due to changes in angular velocity. The raises in the flow rate can not overcome growth in the centripetal field, which made the bubble velocity decrease compared to the former situation.

Although the drift-flux model proposed by Biazussi (2014) [8] presented good results for several flow conditions, it used correlations from Shoham (2005) [14] to relate the velocity field instead of measuring them. The present study differs from Biazussi in this point and, besides, the terms related to the acceleration of gravity were replaced by centripetal acceleration, not being included as a source term in momentum equation. Another difference is in the

starting point of the formulation for the drift-flux model.

Monte Verde et al. (2017) [12] performed an experimental study of gas-liquid flow inside an ESP impeller. The authors reported the gas locking and surging conditions to the flow patterns observed inside the impeller, which were classified by them in Bubble Flow, Agglomerated Bubble Flow, Gas Pocket Flow and Segregated Flow. Their experiments were performed using a high-speed camera and the same visualization prototype used in this study. It was observed that for higher rotational speed, the value of the no-slip gas void fraction increases, and the transition of flow patterns occurs.

Cubas (2017) [15] carried out a study with the gas-liquid mixture in a radial impeller using a high-speed camera. The images obtained were associated with the instabilities observed in the performance degradation in two-phase flow operation under surging conditions. Four flow pattern were observed, as suggested by Gamboa (2009) [11] and Monte Verde (2017) [12]. The gas void fraction was measured using a wire mesh sensor installed at the intake of the pump. The results of the void fraction presented discrepancy compared to the homogeneous model. Cubas (2017) [15] concluded that this difference occurs because the homogeneous model does not consider the slip velocity. In cases where the gas void fraction was higher than BEP, the bubbles had a tendency to flow at the suction blade side. However, considering most of the cases, the bubbles change their direction in the middle of their way or near the impeller outlet going directly through the pressure suction side.

Stel et al. (2019) [16] studied the gas-phase behavior numerically and experimentally. The main components were replaced by transparent components that allow the use of the high-speed camera. The numerical capability was explored to evaluate bubble trajectory, comparing how it is affected by some variables, such as bubble diameter and liquid flow rate. A Lagrangian solution was used to calculate the motion of individual bubbles inside the pump, considering drag, virtual mass, pressure gradient and rotational forces. In his tests, the lift force showed a negligible effect compared to other forces, so it was not considered. In conclusion, bubble trajectories were sensitive to bubble diameter. In addition, the virtual mass can be reasonably high in regions of high-velocity gradients.

The flow inside a multistage ESP model is highly influenced by stage-to-stage transition, impeller-diffuser interaction, and part-load operation. Several other factors, such as turbulence, high viscosity liquid, and two-phase flow inside an ESP deserve detailed studies on their own, since all of them are responsible for key influences on pump performance and until now there is no unique model closed to represent all phenomena.

The aim of the present work is the measurement of velocity and diameter of air bubbles inside the ESP. A high-speed camera was used and a two-phase flow composed of air and water was investigated. An image processing code was written to identify the moving bubbles and compute the velocity of them changing while crossing the impeller, as the diameter as well. With the velocity field of bubbles, a drift-flux model was proposed and a transition criteria for surging and gas locking conditions was proposed, as well.

The present study relates a drift-flux using blade coordinate system, using Navier-Stokes equation and taking into account the velocities in $\hat{r}$ and $\hat{\theta}$ direction. A better comprehension of the phenomena can bring better designs for ESP, such as improved geometries that deal better with gas-liquid flows in the impeller.

2 | EXPERIMENTAL PROCEDURE

Experiments were performed at the Experimental Laboratoy of Petroleum - LabPetro at the Center for Petroleum Studies - CEPETRO, inside the University of Campinas (UNICAMP) in Brazil. The prototype construction was based on a P23 model used in oil production, described in detail by Biazussi (2014) [8]. Monte Verde et al. (2017) [12] built the prototype doing some modifications on P23 model in order to visualize the flow inside the pump. It was necessary

to remove the steel shroud and replace it with an acrylic one, keeping its feature closed. The diffuser was modified for a voluta, letting the impeller exposed. The intake of the impeller remains the same, without modifications in order to orient the flow. A detailed description of the prototype already exists in Monte Verde et al. (2017) [12] study, so only the necessary for the reader is exposed here, which is related to the visualization equipment. For a detailed description, please see Monte Verde et al. (2017) [12].

The high-speed cameras have been widely used in multiphase flow visualization and analyses, such as liquid-liquid, gas-liquid, liquid-solid, among others (Penteado et al., 2016 [17]). As an advantage, this method is precisely and non-intrusive. However, its limitation is related to the necessity of optical access to the process and this rarely happens in turbomachinery, because the fluid was frequently under high pressure.

A high-speed camera of CMOS (Complementary Metal Oxide Semiconductor) type was placed in front of the pump to record the two-phase flow in the impeller (Fig. 1). A camera model Phantom VEO 640S, capable of 4 megapixels with a resolution of $2560\,px \times 1600\,px$ at frequencies up to 1.400 Hz was used. Above these values the quality gradually decreases. A computer controlled the frequencies and exposure times of the high-speed camera and stored the acquired images. The images were stored in cine format, which was opened with the software Phantom CV 2.8 and then converted to avi format. In our tests, we set frequencies to values within 1000 *Hz* for 600 rpm, 1500 *Hz* for 900 rpm and 2000 Hz for 1200 rpm. Those values were set up according to the quality of the image obtained from 1200 rpm, which has its resolution of $1536\,px \times 1536\,px$ keeping 4 megapixels.

The camera was set up in the same place used by Monte Verde (2017) et al. [12], but using a different illumination. High-speed cameras demand an efficient illumination, due to higher frequencies acquisition. In other words, it means that the object should not have shadows in the capture time. Three sources containing 24 LED (Light-Emitting Diode) lamps each were used to provide a constant illumination. Their input wattage was 84 Watts and delivered 7.700 lumens of brightness each one. For the tests, the number of acquired images were around 7.400 and 15.000 frames, and a Canon lens f/1.4 of $50\,mm$ focal distance was used. The images were recorded in gray-scale format. An example of movie showing the motion of bubbles is available as Supplementary Material.

Figure 2 indicates the experimental campaign realized. The experiments related to single-phase flow (SPF) are placed to compare the single-phase with two-phase pump performance. Although some of these tests did not use the high-speed camera, they were done to verify the pump performance, comparing the data with the experiments from the literature, such as Gamboa (2009) [11] and Monte Verde (2016) [18]. The four patterns observed by them occurred in the present study.

The two-phase flow experiments were conducted using tap water and compressed air as working fluids. The air mass flow rate was kept constant. Sixteen tests were performed using the high-speed camera in 600, 900 (one was repeated with different mass flow rates), and 1200 rpm. The first tests were performed with 0.0125 kg/h gas mass flow rate. We observed that, when increasing the gas flow rate to 0.0250 kg/h the quality also increases.

TABLE 1 Test matrix for the experimental campaign.

Rotation	Water mass flow rate	Air mass flow rate
600 rpm	710 to 3310 kg/h	0.025 kg/h
900 rpm	833 to 5273 kg/h	0.025 kg/h
900 rpm	1200 to 5240 kg/h	0.012 kg/h
1200 rpm	798 to 7141 kg/h	0.025 kg/h

Therefore, the next twelve experiments were done with 0.0250 kg/h. Rotations above 1200 rpm cause the

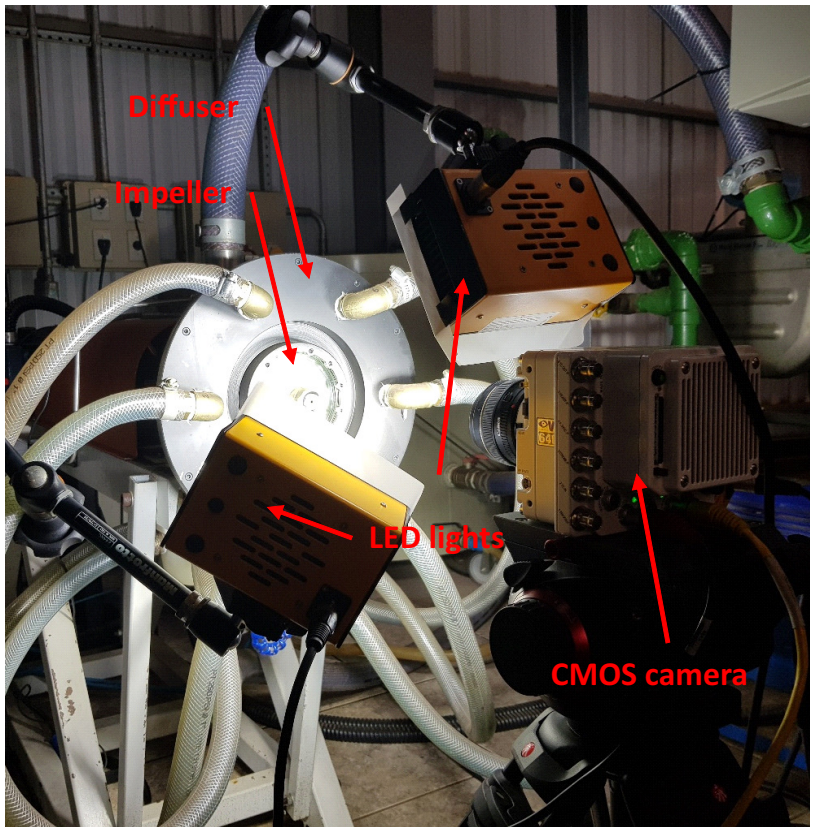

FIGURE 1 Main components in the experimental setup: Pump impeller and diffuser, LED lights and CMOS Camera.

impeller to break the bubbles so much that they seem like a cloud. In this condition, they have so many shadows (in our case, it represents noise) that detecting any bubble displacement was not possible. The suction pressure was set up in 150 kPa. Table 1 shows the test matrix. A description of the image post-processing is shown in the next subsection.

2.1 | Post-processing of images

Numerical scripts wrote by the authors processed the images acquired in the course of this study. The code written must capture the displacements of the bubbles and then find their velocities. Image post-processing was divided in two main steps. First, the code identifies the regions where bubbles were moving. In the second stage of the code, bubble displacements were acquired. The steps of the first part of the code are:

1. Image rotation.
2. Region of Interest (ROI).
3. Adaptive histogram.
4. Strel filter.
5. Image subtraction.
6. Wiener filter.

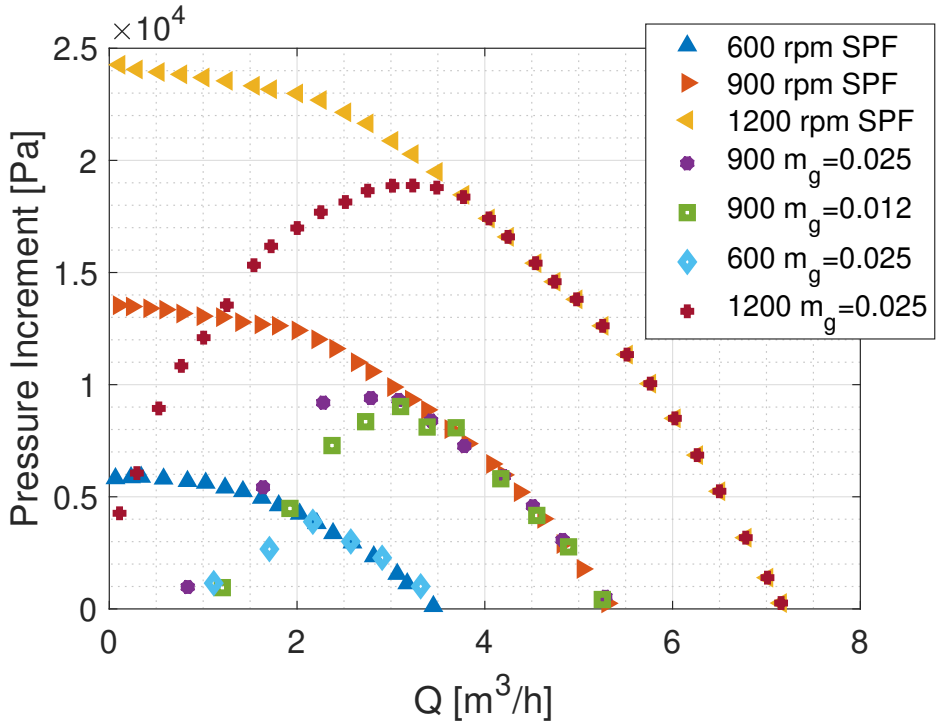

FIGURE 2 Pressure Increment x Flow rate Graph of the Experimental Campaing for single-phase flows (SPF) and two-phase flows.

7. Laplacian filter.
8. Binarization.
9. Median filter.
10. Eccentricity filter.
11. Cell formation.
12. Pairing.

The camera remained frozen when capturing the images, which means that the code needs to rotate the image to capture only the displacement of the bubble. The frequency represents how much the impeller rotates from one frame to another. With this information, the image needs to be rotate at:

$$I = \frac{\omega}{60}\frac{360}{fr} \tag{1}$$

where ω is the rotation of the impeller in rpm and fr is the acquisition frequency of the camera in Hz. The result of I in Eq. 1 corresponds to 3.6° degrees of rotation from the first image captured to the following one. For all the tests the acquisition frequency is adjusted for the camera to take a shot every 0.24 seconds. This is the sampling interval. The next step was the creation of a Region of Interest (ROI).

Figure 3(a) represents the image acquired from the tests for $q_l = 4.511\ m^3/h$ and $q_g = 0.025\ kg/h$, and the borders in blue separate the unnecessary pixels. In image post-processing this represents the mask (Oppenheim and Schafer, 2014 [19]). With the mask representing the region of interest (ROI) the pixels outside it are replaced by the value 0, which means that it appears as black. The cropped image is shown in Figure 3(b) .

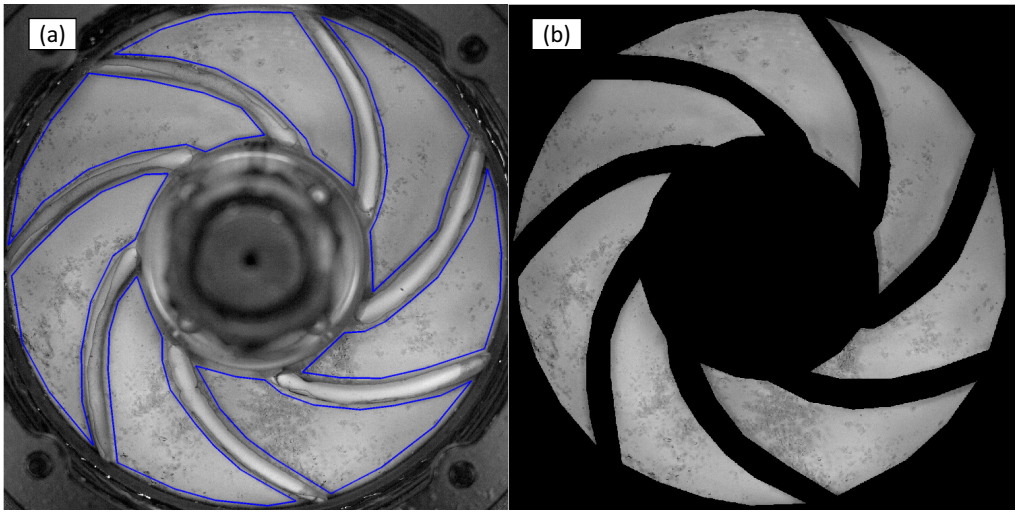

FIGURE 3 Image of gas-liquid flow inside the Impeller: (a) Real Frame and ROI (blue borders); (b) Cropped image showing only the impeller channels.

The creation of the ROI is an essential process because the scripts applied in the sequence have the guarantee that displacements of bubbles receive the next filters without the noise of unnecessary pixels. The next scripts count with techniques used in spatial processing.

The intensities of a pixel can be changed according to the neighboring pixels' intensities by a technique called spatial filtering. An image is a two-dimensional function, $f(x, y)$ where x and y are spatial coordinates and the amplitude of f at any pair of coordinates (x, y) is called the intensity of the image at that point. In our case, the output (processed) image is $g(x, y)$, and T is an operator on f defined over a specified neighborhood of point (x, y). The spatial domain processes are denoted by Eq. 2.

$$g(x, y) = T[f(x, y)] \tag{2}$$

The original image $f(x, y)$ receives the treatment of an operator, $T[\cdot]$, such as the median filter. After that, the new image is $g(x, y)$. The intensity values acquired in gray-scale correspond to values between 0 (black) or 255 (white). In signal processing, noise is characterized as any information that blurs the object, an undesirable aspect such as small changes in illumination that may occur in our case. The script uses adaptive histogram equalization (AHE) to improve the contrast in images (Gonzalez and Woods, 2008 [20]). Its function redistributes the lightness values of the image. Therefore it improves edge definitions in each region of an image.

Seven channels are noted in Fig. 3(b). The external observation, which can be done by the operator who is making the code, have more quality in the analysis if the image window is amplified. This means that a reduced window improve the details of images, working as a zoom or amplification lens. Figure 4 and 5 explains better to the reader what this means as they are showing only a channel of the impeller. Further details are provided by Fig. 16 in Appendix B.

Morphological operations as dilation and erosion were executed in Matlab. The strel filter is a morphological operation that uses a disk-shaped structuring element in the present study. Typically, the structured element selected

should be the most similar to bubble shape and have the nearest size to improve the effectiveness of this operation.

The next operation is the image subtraction, a similar process that was conducted by Penteado and Franklin (2016) [17]. Two consecutive images were necessary to execute this script, which indicates the possible displacements that occurs. This script goes a little further in the code steps, so that it executes the Wiener, Laplacian and Binarization process to then return the values acquired. That is the reason why Fig. 4 is already showing the bubble's centroids. The red circles indicates the current frame, the blue squares, the next frame, and the green markings indicate the location of possible displacement as a result of the script.

Thus Fig. 4(a) shows the process without the use of image subtraction. The centroids had already been calculated in two consecutive images and plotted. Fig. 4(b) shows the filter acting and removing some centroids where no displacement occurred. The centroids removed were shown by a blue arrow in Fig. 4(a).

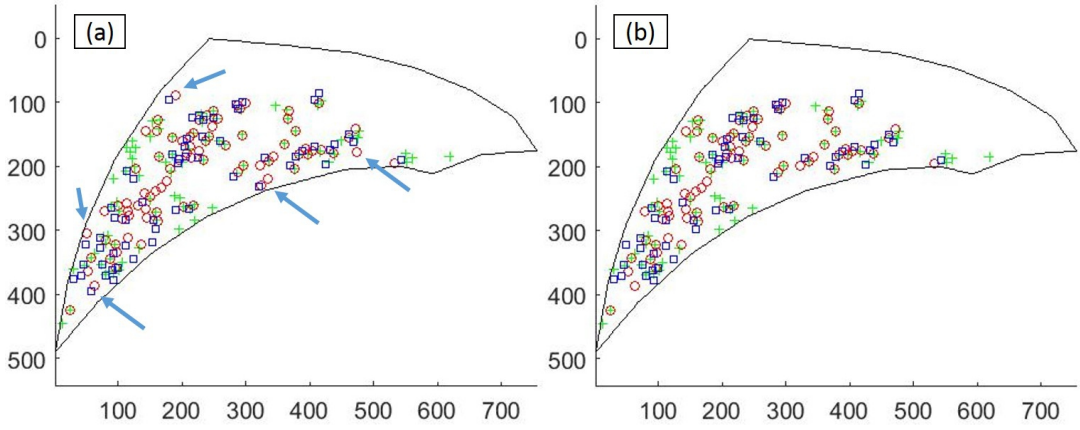

FIGURE 4 Analysis of bubble displacement, Red circles indicate the current frame, the blue squares, the next frame, and the green markings indicate the location of possible displacement: (a) Bubbles Centroids - each symbol/color represents a bubble displacement; (b) Subtraction of no-movement centroids applied.

Wiener deconvolution is a process to deblur the images, reducing their noise. Small changes may occur in illumination due to the rotation of the impeller. Right at the center of it, the pump's axis does some shadow, and even with the best effort to try a better positioning for illumination, a small portion of shadow remains in some areas; therefore, Wiener deconvolution decreased this effect.

The Laplacian filter was employed after the Wiener deconvolution. It is a linear spatial filter used to emphasize image contrast. It allows to enhance bubble contours. Considering this situation, two types of spatial masks to enhance edges were tested and the one that showed the best result is given by the matrix showed in Eq. 3.

$$\text{Spatial mask:} \quad \begin{bmatrix} 1 & 1 & 1 \\ 1 & -8 & 1 \\ 1 & 1 & 1 \end{bmatrix} \qquad \text{Laplacian:} \quad g(x,y) = f(x,y) + c\left[\nabla^2 f(x,y)\right] \tag{3}$$

The Laplacian of an image $f(x,y)$, denoted $\nabla^2 f(x,y)$, is defined by Equation 3. This expression was implemented at all points in the image, convolving with the spatial mask that considers diagonal elements. The enhanced image is given by $g(x,y)$, and c is 1 if the center coefficient of the mass is positive, or -1 if it is negative (Gonzalez and Woods, 2008 [20]). Figure 5(a) and (b) show the comparison between an original image and the enhanced one. To apply this

filter, the image class was changed, letting intensity numbers in the range from 0 to 1, which corresponds to 255. Values near 0 were considered black, even negative values.

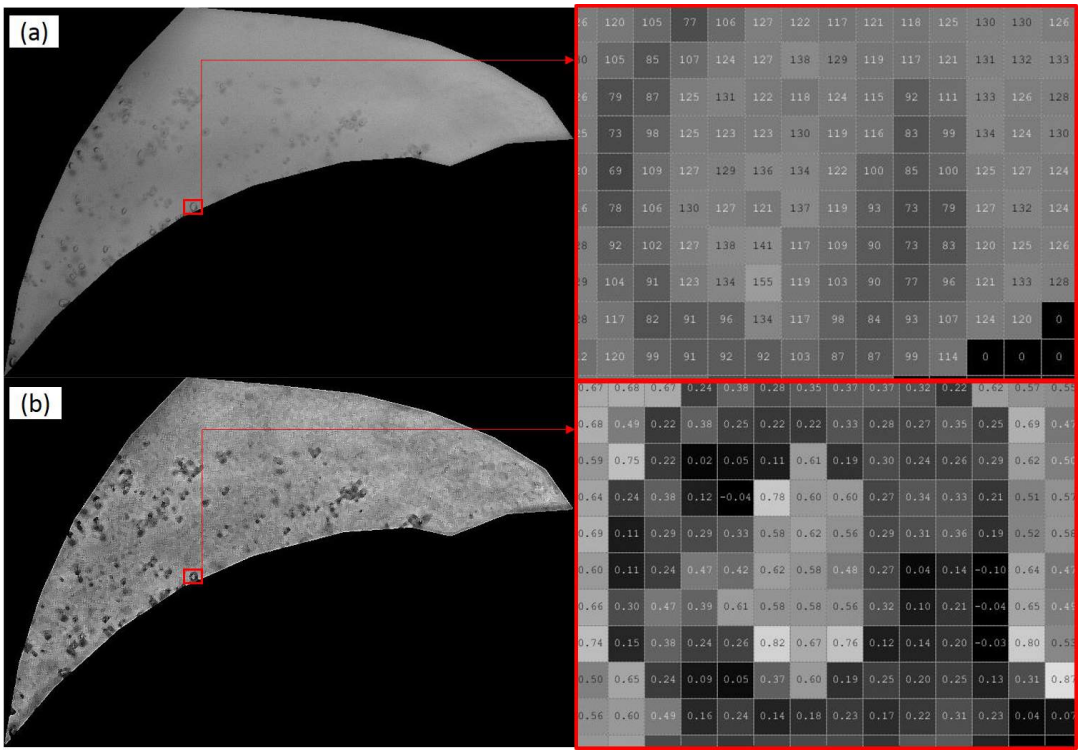

FIGURE 5 Application of Filters to an Image: (a) Original Image; (b) Image with Laplacian filter applied.

The borders of bubbles in Figure 5 were prominent in the comparison, which increases the efficiency when binarizing the frames. The Binarization process has a threshold value between 0 and 255, changing the color of divided pixels into black, 0 or white, 1 (Sonka et al., 2014 [21]). A median filter was applied, reducing noise. Each output pixel contains the median value in a 3-by-3 neighborhood around the corresponding pixel in the input image, symmetrically extending the image at the boundaries.

The resulting matrix contains values of pixel intensities of 0 and 1. The black values inside the mask indicate the bubbles, where the values corresponding to 1 are white. This matrix is submitted to a filter called "area filter", inside the same script. It consists of removing regions with an area smaller than a threshold value ($5\ px^2$ in our experiments), i.e., values lower than this were changed from 0 to 1 inside the binarized matrix.

Furthermore, a binarized image has regions formed by the bubbles. Some parameters are acquired, such as area, perimeter, hydraulic diameter, eccentricity, and others. The variable "eccentricity" is useful for comparing with the bubble's circumferential shape, and it is used in a filter known as eccentricity filter. High values are not expected, thus they were excluded from the analysis. The threshold of .95 was arbitrarily chosen, so that values above it were removed.

Finally, the information acquired from the first part of the code was saved in a cell array inside Matlab. In our

case, four variables were saved: diameters, bubble position, size of the matrix, and the sum of the bubble's area in the impeller channel. The next section reports the code calibration, which certifies the data acquired.

2.1.1 | Bubble trajectories: code calibration

Many variables may change bubble velocity in the impeller of an ESP, such as the rotational velocity, characteristics of the flow, among others. By this reason, the present impeller does not have a parameter for bubble velocity, thus, the trajectories of air bubbles were acquired manually from image post processing and the results were shown in Fig. 6. The process to acquire them was conducted analyzing image by image and writing the position of the bubbles in that time. This process demands an extensive time for each bubble to be followed, about four hours.

First, it is necessary to find a bubble that starts its trajectory from the impeller's entrance. Then the position is written and the velocity is acquired. In Fig. 6(a) it is possible to see some bubble trajectories in red, crossing the channels of the impeller, represented by the mask in blue. The axis of the figures was plotted using the pixel scale, and it is not converted to meters. As already discussed by other authors, the bubble trajectories are random and do not follow a unique pattern (Monte Verde et al., 2017 [12]).

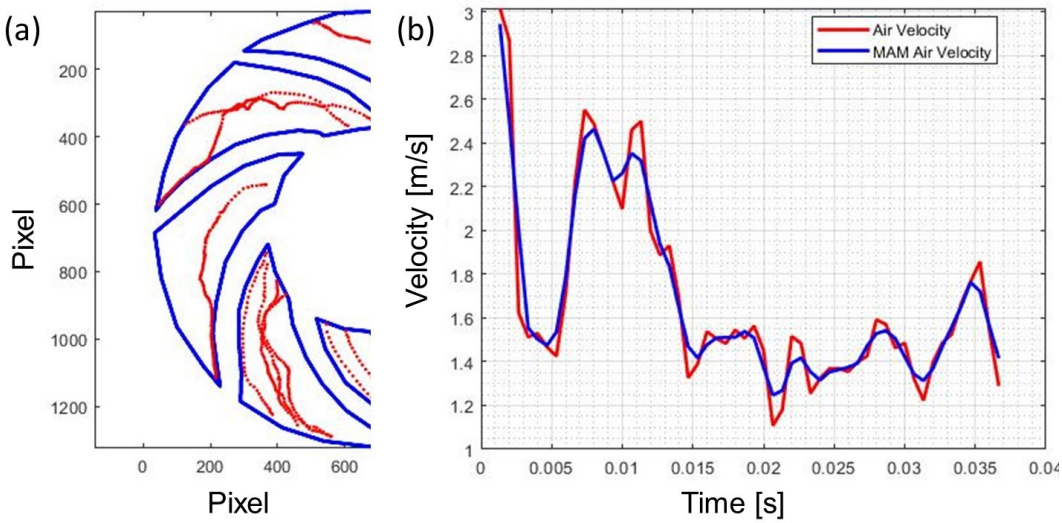

FIGURE 6 (a) Examples of bubble trajectories in the impeller channel - (b) Velocity fluctuation of a bubble with 0.5 mm diameter through the impeller channel.

Each experiment was calibrated at the beginning to make sure that the camera did not change its position, even slightly. Most of the images captured in this study showed a relation where 1 millimeter is equivalent to 11.8 pixels, rounded to 12 - supposing a bubble moving at 1.00 m/s or 12 pixels between two frames acquired at 1500 fps. If the velocity of the bubble changes to 13 pixels between an image pair, it accelerates to 1.08 m/s. The higher fluctuations of velocity can be considered uncertain when capturing the bubble centroids.

$$v_{MAM} = \frac{v_{i-1} + v_i + v_{i+1}}{3} \tag{4}$$

Therefore the velocity is considerably affected by small changes in pixel position. A single pixel error in the tracking process can propagate and become larger errors when calculating the velocities and accelerations. This effect may be reduced by applying the moving average method (MAM), represented by Eq. 4. The higher velocity fluctuations were attenuated when MAM was used. Fig. 6(b) shows the velocity captured without and with MAM (smoothed), represented by the red and blue lines, respectively.

2.2 | Experimental Results

The Cell data acquired from the first part of the code is addressed in this section. One must open in another script to reduce the memory and storage for all those images processed in Matlab. It is vital to organize the data in the current and next frames. These matrices must have the same index because the same bubble needs to be tracked throughout the impeller channel. This is known as pairing process. In other words, pairing can be known as a bubble in the current frame being analyzed as the same bubble in the next frame after a specific time given by the image frequency acquisition.

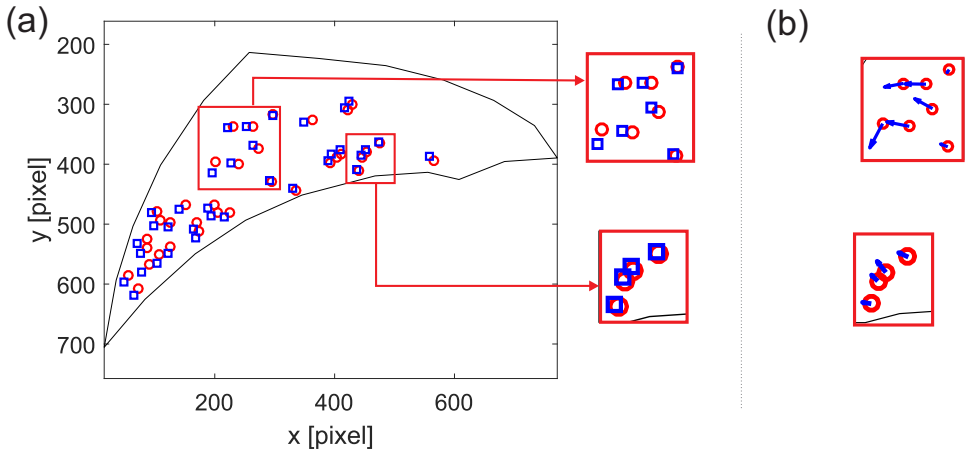

FIGURE 7 Pairing process results for bubble: (a) Pair of bubbles centroids and (b) velocity vectors.

The pairing process demands a comparison between both matrices. When the code is searching for a pair from a specific index of the current frame (or matrix) and this pairing process fails, this means two possibilities: that the bubble goes out of the impeller or that the "bubble" is not a bubble, but a noise, and can be discarded. The possible pairs were only accepted after this script, which is related to the position expected from that bubble. Index by index of the current frame is done repeatedly for the sequence of images.

After that, the subtraction between the matrices was done, and the displacements were acquired. Figure 7(a) shows the centroids from the current frame at time $t1$, represented by red circles. The centroids from the next frame at time $t2$ are represented by blue squares.

In possession of the displacements and the acquisition frequency fr, the velocities were obtained. For an example, the data showed in Figure 7(a) can be represented as velocity vectors of air bubbles in a pair of images, as showed in Figure 7(b). The direction of the vector and its module are indicators for the paring process. These values should have a parameter to be compared, which was made in next section, *Bubble trajectories: code calibration*. Besides the

velocities, the code also computes the bubble's area in the impeller, allowing the possibility to calculate the gas void fraction.

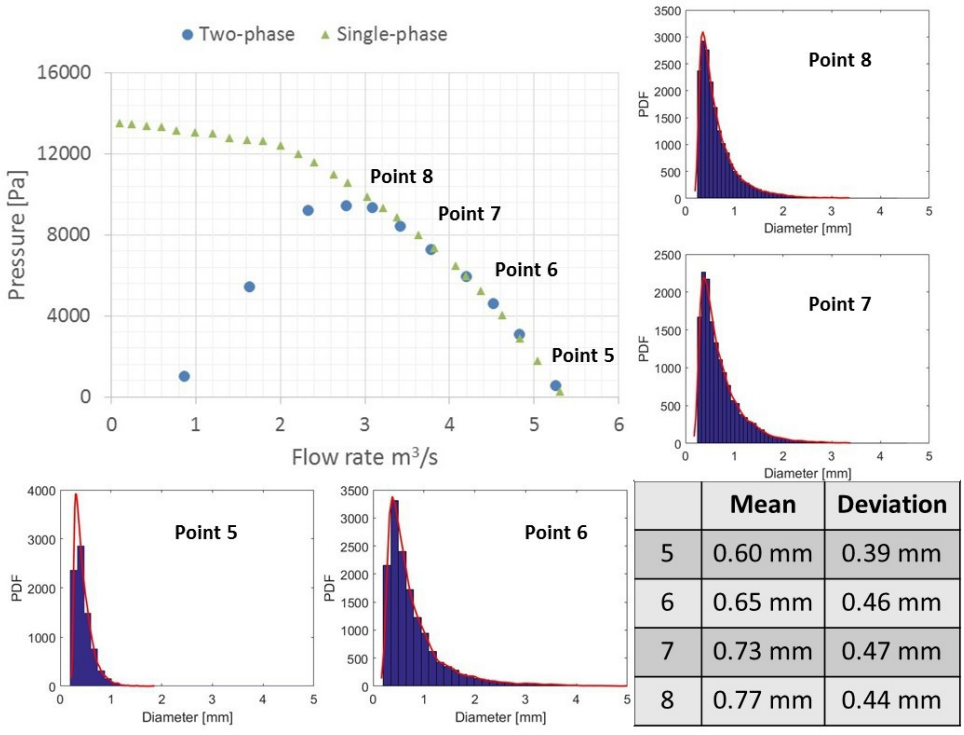

	Mean	Deviation
5	0.60 mm	0.39 mm
6	0.65 mm	0.46 mm
7	0.73 mm	0.47 mm
8	0.77 mm	0.44 mm

FIGURE 8 Experiments in the pressure x flow rate chart, and histograms indicating the diameter from points 5 to 8 - 900 rpm and 0.025 kg/h changing liquid flow rate.

The value of gas void fraction, α_{exp}, is calculated using the hydraulic diameter of each bubble. The bubble's volume was approximated using the sphere's volume, once the images acquired were at a 2D format. The sum of the bubbles' volume divided by the channel volume is equal to alpha. This data showed a high variation along the timestep (or fps) which indicates that bubbles sometimes appear in swarms inside the impeller channels. Due to this, the volume expected for the bubble changes with time, as they are approached using the sphere's volume. The mean values of gas void fraction α_{exp} calculated by the code for each experiment were compared by the ones calculated using the model and they are discussed in section *General discussion*.

The main objective of the code is to treat a great number of data, which is unpractical to do manually due to the time demanded. Sixteen tests were made, dividing each in seven because of the number of impeller blades. Each channel has 1874 images analyzed and their results were reunited in a single file to get an average result. More than that, a probability distribution function (PDF) was created for velocities and diameters of the air bubbles for each test. The results are shown in Fig.8). The distribution that fitted the data was a nonparametric representation (Hinkelmann and Kempthorne, 1994 [22]).

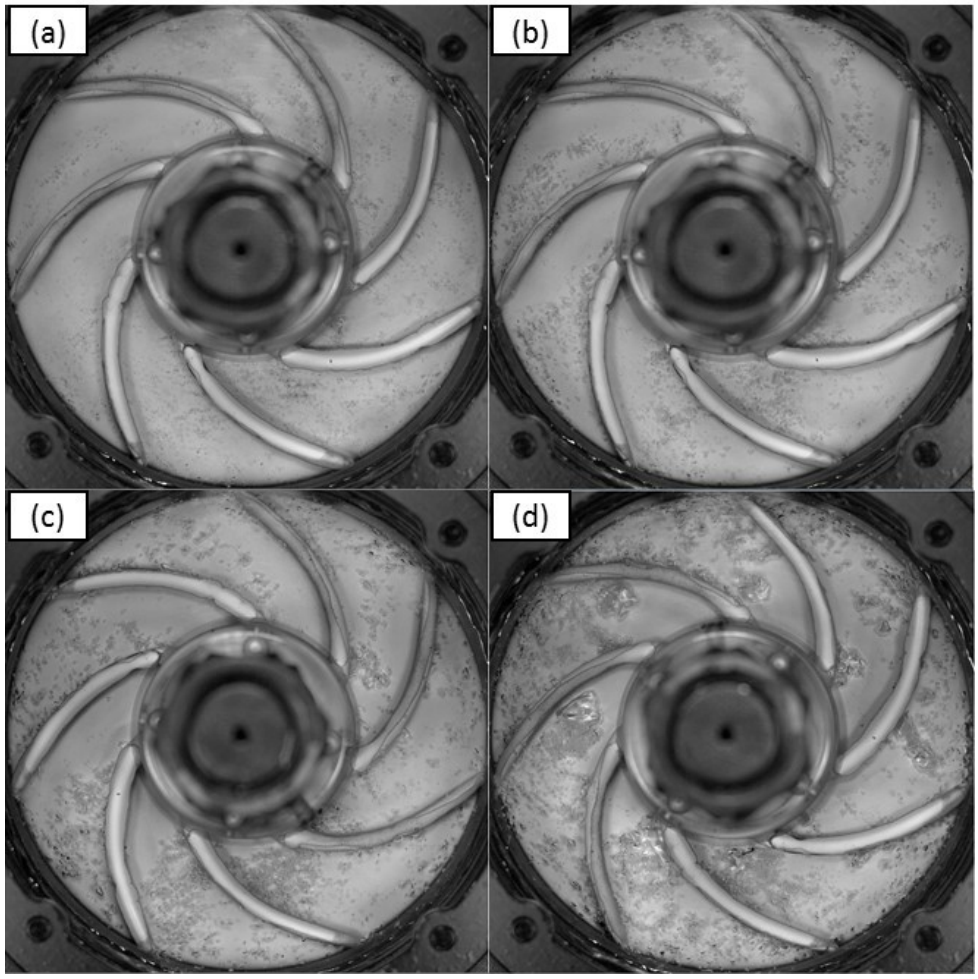

FIGURE 9 Snapshots of the gas-liquid flow inside the ESP (refer to Fig.8 for flow conditions): (a) Point 5 (b) Point 6 (c) Point 7 (d) Point 8 - 900 rpm and 0.025 kg/h at different liquid flow rates.

In Fig. 8, the chart on the top indicates *Pressure increment* by *Water flow rate*, which gives an idea of how much gas is inside the impeller. When the water flow rate decreases, more gas can be observed in the experiments. The points in Fig. 8 were represented in Table 2 and their images are shown in Fig. 9. The motion in these experiments can be seen as Supplementary Material. Besides, a table on the left, below Fig. 8 indicates the results of the PDFs done for the diameters of the air bubbles and their respective points.

As expected, bubble diameter increases when the liquid flow rate decreases. The quantity of bubbles multiplies, raising the swarm effect inside the impeller channel. This swarm increases the coalescence of bubbles as they are closer. The images in Fig. 9 indicate this phenomenon. The coalescence increases the size of the bubbles and their deviation because a bigger bubble population exists inside the impeller channel. Point 8 is near the pump inflection curve, which is the beginning of the unstable condition known as surging.

TABLE 2 Impeller rotation ω, mass gas flow rate $\dot{m}$, diameter d, pressure increment ΔP, radial velocity v_r, circumferential velocity v_θ, standard deviation of radial velocity δv_r and standard deviation of δv_θ.

Exp.	ω	$\dot{m}$	d	ΔP	v_r	v_θ	δv_r	δv_θ
	$[rpm]$	$[kg/h]$	$[mm]$	$[Pa]$	$[mm/s]$	$[mm/s]$	$[mm/s]$	$[mm/s]$
1	600	0.025	1.4	1007	759	876	217	223
2			1.4	2280	682	857	242	261
3			1.6	3006	606	864	211	240
4			1.6	3886	534	821	238	269
5	900	0.025	0.6	541	1021	1425	245	298
6			0.6	4579	969	1346	257	276
7			0.7	7260	868	1283	303	324
8			0.8	9318	825	1172	332	350
9	900	0.012	0.6	419	1028	1447	292	336
10			0.6	4168	980	1342	286	301
11			0.7	8078	862	1296	312	388
12			0.9	9025	769	1211	271	315
13	1200	0.025	0.4	262	1527	1806	318	346
14			0.4	5246	1497	1759	341	355
15			0.5	11341	1395	1668	319	329
16			0.6	16589	1291	1425	295	329

Table 2 shows the mean values for standard deviation of radial and circumferential velocities for bubbles in each test run. The table also presents the rotational velocity ω, mass gas flow rate $\dot{m}$, bubble diameter d, pressure increment ΔP, radial velocity v_r, circumferential velocity v_θ, standard deviation of radial velocity δv_r and standard deviation of circumferential velocity δv_θ.

All the velocities increased along with the rotation velocity, which is expected because more energy has been added to the fluid. The standard deviation also increased. The diameter of the bubble act in an opposite way, the increase in energy provokes an increase in bubbles break-up, thus reducing their diameters. The different values of the gas flow rate do not bring a considerable difference in the velocities. Perhaps the gas flow rate should present a higher difference between them to show considerable changes in velocities. Further experiments should be conducted to test this. Considering the pressure values, when it rises for the same value of pump rotation, the velocities decrease. Besides, in this Table, the lower values for pressure indicate high values for the water flow rate.

The velocity data acquired in the experiments and present in Table 2 were used to close the Drift-flux model, described in section *Model description*.

3 | MODEL DESCRIPTION

The geometry of a rotodynamic machines consists of a set of rotor blades attached to a hub and operating within a static casing. The impeller was modeled using the concept of a radial cascade (Brennen, 2011 [23]), represented in Fig. 10. This figure used three blades to better represent the notation used for the pump impeller.

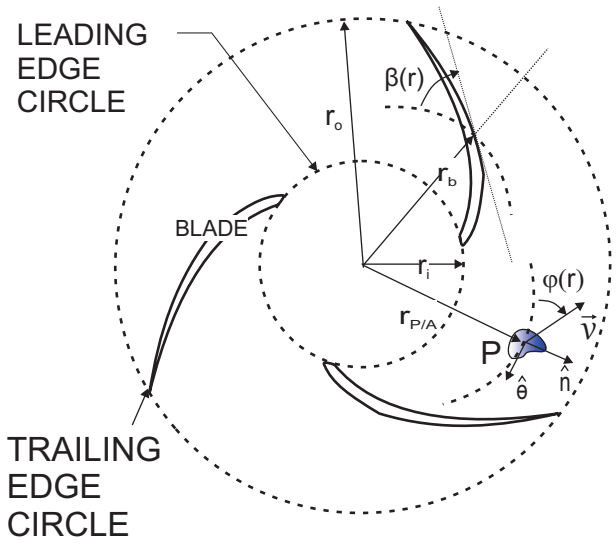

FIGURE 10 Radial cascade of the impeller (Brennen, 2011 [23]).

The angle $\beta(r)$ is related to the blade angle associated to $\hat{\theta}$-direction. The velocity represented by the letter v is the velocity of a flow particle **P** in non-inertial frame of reference. A detailed description of the kinematics of the movement is in Appendix C, in the section Kinematics for rotor dynamics. The angle φ is the angle of velocity $\vec{v}$ associated to $\hat{\theta}$-direction. The inner/entrance and outer/exit radius are defined as r_i and r_o, respectively, and the subscript b refers to the blade.

The development of the drift-flux model formulation in this study uses the mass and momentum equations and they are developed considering a specific set of operations of an electric submersible pump (ESP), including a two-phase gas-liquid flow where subscript 1 and 2 were used for the liquid and gas phases, respectively. The letter k was used to represent the phases in the equations. To start the calculations some hypothesis were assumed:

- Incompressible flow;
- No mass transfer between the phases;
- Constant local properties (thermal conductivity, specific heat, no fluid thermal expansion);
- Viscosity is function of the temperature only;
- Steady state;
- Neglecting superficial and interfacial tension;
- Assuming no variation in z-direction;
- Neglecting hydrofoil thickness.

The real structure has blades whose set form a hydrofoil distorted with its camber mean line following a logarithmic spiral. The polar coordinate system was changed to blade coordinate system ($\hat{s}$ and $\hat{n}$), and this development is expressed in Appendix C, in the section *Blade coordinate system*. The rotation matrix is used to transform the coordi-

nates between the system.

Further, radial pumps can be approximated as a channel that has a variable cross-section, meaning that the cross-sectional area at the entrance is different from the exit. Besides, the channel has a curvature and its structure is axisymmetric, thus the description was done by just one channel. Considering the hypothesis already exposed, the model begins with differential equations written in polar coordinates. Before the reader starts the next sections, it is recommended to see *Appendix C. - Math tools*, where the entire explanation for coordinate system change and the initial steps for turbomachinery are described.

3.1 | Continuity Equation

Considering the assumed hypothesis the continuity equation for each phase can be written as in Eq.5.

$$\frac{1}{r}\frac{\partial}{\partial r}(\alpha_k \rho_k r v_{kr}) + \frac{1}{r}\frac{\partial}{\partial \theta}(\alpha_k \rho_k v_{k\theta}) = 0 \tag{5}$$

The volumetric flux of each phase, j_k, is given by (Ishii and Hibiki, 2010 [24]):

$$j_k = \alpha_k \, v_k \tag{6}$$

Considering the premises:

- Incompressible flow, which means Mach $\ll 1$.
- The velocity variation through the impeller in r direction from Eq. 6 was written in its weak form for azimuth direction. It was integrated in θ direction and no-slip condition was considered. Terms $j_{k\theta}(\theta_1(r))$ and $j_{k\theta}(\theta_2(r))$ are null.
- The terms in θ were modeled as an average value letting the variables in function of radius. The average value in θ was calculated using the Leibniz's rule.
- In order to obtain the average operator, the equation was multiplied by $1/\Delta\theta$.
- Defining $(1-\lambda) = Q_1/Q_m$, and $\lambda = Q_2/Q_m$ and the mixture flow rate as $Q_m = Q_1 + Q_2$ (Ishii and Hibiki, 2010 [24]).
- The bar above or the brackets used in the expression means an average value.
- The volumetric flux or superficial velocity is $j_{kr}(r) = Q_k/A(r)$. The mixture volumetric flux is defined as $j_m(r) = Q_m/(2\,\pi\, r\, h)$

The entire development for Eq. 5 is shown in Appendix A, in section 5. Considering the velocity triangle for turbomachinery, a relation between $j_{kr}(r)$ and $j_{k\theta}(r)$ can be obtained which is $v_{k\theta}(r) = -v_{kr}\cot\beta$. This is showed in Eq. 7. So:

$$\begin{aligned} j_{kr}(r) &= \alpha_k(r)\, v_{kr}(r) \\ j_{k\theta}(r) &= \alpha_k(r)\, v_{k\theta}(r) = -\alpha_k(r)\, v_{kr}\cot\beta = -j_{kr}(r)\cot\beta \end{aligned} \tag{7}$$

The radial and azimuth slip are given by, respectively (Ishii and Hibiki, 2010 [24]):

$$v_{sr}(r) = v_{2r}(r) - v_{1r}(r) = \frac{j_{2r}}{\alpha_2} - \frac{j_{1r}}{\alpha_1} = j_m(r)\left[\frac{\lambda_2}{\alpha_2(r)} - \frac{\lambda_1}{\alpha_1(r)}\right] \tag{8}$$

$$v_{s\theta}(r) = v_{2\theta}(r) - v_{1\theta}(r) = \frac{j_{2\theta}}{\alpha_2} - \frac{j_{1\theta}}{\alpha_1} = -j_m(r)\left[\frac{\lambda_2}{\alpha_2(r)} - \frac{\lambda_1}{\alpha_1(r)}\right]\cot\beta \tag{9}$$

The system coordinates were developed in Appendix A, in section 5. Appendix C, section 5 developed the velocity components for turbomachinery. Due to the velocity field premises stated, the slip on normal direction to $\hat{s}$, represented by $\hat{n}$ is null. The velocity field was simplified with this hypothesis. So:

$$v_{s,s}(r) = v_{sr}(r) \Big/ \sin\beta \qquad \text{or} \qquad v_{sr}(r) = v_{s,s}\sin\beta \tag{10}$$

Hence, estimating v_{sr} it is possible to find $v_{s,s}$ which is desired. The polar coordinate system can be change to the blade coordinate system, so the velocity vector is represented by: $\vec{v} = v_s\hat{s} + v_n\hat{n}$. So the velocities in direction $\hat{s}$ and $\hat{n}$, v_s and v_n are, respectively:

$$v_s = v_r\sin\beta - (-v_r\cot\beta)\,\cos\beta = v_r\left(\frac{\sin^2\beta + \cos^2\beta}{\sin\beta}\right) = \frac{v_r}{\sin\beta} \tag{11}$$

$$v_n = v_r\cos\beta + (-v_r\cot\beta)\,\sin\beta = v_r\cos\beta - v_r\frac{\cos\beta}{\sin\beta}\sin\beta = 0 \tag{12}$$

Therefore, as the slip had the same projections and the same components, the result of Eq. 11 and 12 must be equal for slip, i.e.: $v_{s,s} = v_{sr}/\sin\beta$ and $v_{s,n} = 0$. These results are important in the development of this model because with the simplifications already made, these results show that there is only slip in the main direction of the flow, which is in $\hat{s}$. Besides, the slip in $\hat{n}$ clearly is equal to zero, as expected. The volumetric flux is $j_k = \alpha\,\vec{v}_k$ (Eq. 6) and the same projections of $\vec{v}$ are applied to $\vec{j}$, so:

$$v_{s,s} = v_{2s} - v_{1s} = \frac{j_{2s}}{\alpha_2} - \frac{j_{1s}}{\alpha_1} = \frac{(1-\alpha)\,j_{2s} - \alpha\,j_{1s}}{\alpha\,(1-\alpha)}$$

$$j_{2s} = \alpha\,(j_{1s} + j_{2s}) + \alpha\,(1-\alpha)\,v_{s,s} \qquad \text{or} \qquad v_{2s} = j_{m,s} + v_{2j} \tag{13}$$

where the Drift-flux velocity v_{2j} is equal to $\alpha\,(1-\alpha)\,v_{s,s}$ and $v_{s,s}$ is the relative velocity or slip velocity. Applying the mean operator in Eq. 13:

$$\langle j_{2s}\rangle = \langle\alpha\,j_{ms}\rangle + \langle\alpha\,(1-\alpha)\,v_{s,s}\rangle$$

where C_0 is the distribution parameter given by:

$$C_0 = \frac{\langle\alpha\,j_{ms}\rangle}{\langle\alpha\rangle\langle j_{ms}\rangle} \qquad \text{and so} \qquad \langle j_{2s}\rangle = C_0\,\langle\alpha\rangle\langle j_{ms}\rangle + \langle\alpha\,(1-\alpha)\,v_{s,s}\rangle \tag{14}$$

The term v_{2s} is obtained by the radial and azimuthal velocities v_{2r} and $v_{2\theta}$, respectively, measured experimentally from the image treatment. In posses of the gas void fraction, they can be related to j_{2s}. Besides, these velocities are shown in section *Experimental Results* and used to calibrate the Drift-flux model. The mixture volumetric flux j_{ms} is acquired from experimental data and this is equals to $j_{1s} + j_{2s}$.

3.2 | Momentum Equation

The momentum equation in radial and azimuth direction were written considering the premises:

- The same hypothesis used for continuity equation were considered here.
- The velocity field has its dependence only to radius, so any $\partial/\partial\theta$ of any velocity is null.
- The gravity acceleration for this case is neglected.
- The momentum received by one phase is equal to the one given by the other, but they have opposite directions, i. e. $\vec{M}_2 = -\vec{M}_1$.
- Fictitious forces are given through fictitious accelerations which already have been calculated. The subscript k is present indicating that they are applied for both phases. $S_k = -\alpha_k\,\rho_k\,\vec{A}_{kf}$ where $\vec{A}_{kf} = A_{kfr} + A_{kf\theta} = \left(2\vec{\Omega}\times\vec{v}_P + \vec{\Omega}\times\vec{\Omega}\times\vec{r}_{P/A}\right)$.
- Both phases have the same pressure: $p_1 = p_2$.

So in polar coordinates the momentum equation are:

- **Radial direction (polar) $\hat{r}$:**

$$\alpha_k\rho_k\left(v_{kr}\frac{\partial}{\partial r}v_{kr} - \frac{v_{k\theta}^2}{r}\right) = -\alpha_k\frac{\partial p_k}{\partial r} - M_{kr} - \alpha_k\,\rho_k\,\vec{A}_{kr} + \nabla\cdot\vec{\vec{\tau}} \tag{15}$$

- **Azimuth direction (polar) $\hat{\theta}$:**

$$\alpha_k\rho_k\left(v_{kr}\frac{\partial}{\partial r}v_{k\theta} + \frac{v_{kr}\,v_{k\theta}}{r}\right) = -\alpha_k\frac{1}{r}\frac{\partial p_k}{\partial\theta} - M_{k\theta} - \alpha_k\,\rho_k\,\vec{A}_{k\theta} + \nabla\cdot\vec{\vec{\tau}} \tag{16}$$

where $\nabla\cdot\vec{\vec{\tau}}$ indicates the viscous stress tensor.

The pressure gradient and the momentum transfer between the phases need to be estimated using the simplified velocity field assumed. The field pressure ΔP can be obtained integrating in r direction. As already showed the slip occurs only in $\hat{s}$-direction which can be estimated with momentum transfer rate in $\hat{r}$ direction.

- **Radial pressure gradient:**

The momentum equation for phases 1 and 2, described by Eq. 15, are added respectively for each phase. As a result, the interfacial momentum transfer are canceled because both have the same module but different directions: $M_{1r} = -M_{2r}$.

$$\alpha_1\,\rho_1\left(v_{1r}\frac{\partial}{\partial r}v_{1r} - \frac{v_{1\theta}^2}{r}\right) + \alpha_2\,\rho_2\left(v_{2r}\frac{\partial}{\partial r}v_{2r} - \frac{v_{2\theta}^2}{r}\right) = -(\alpha_1+\alpha_2)\frac{\partial p}{\partial r} - (\alpha_1\,\rho_1 + \alpha_2\,\rho_2)\,A_{kfr} + \nabla\cdot\vec{\vec{\tau}} \tag{17}$$

The development of Eq. 17 is shown in Appendix A, in section *Radial Pressure Gradient*. The result is Eq. 18:

$$-\frac{\partial p}{\partial r} = \tilde{\rho}_m\left[\frac{(1+\cot^2\beta)}{4\,\pi^2\,h^2}\right]Q_m^2\left(\frac{-1}{r^3}\right) + \overline{\rho_m}\left(\frac{\cot\beta}{\pi\,h}\right)\omega\,Q_m\left(\frac{1}{r}\right) - \rho_m\,\omega^2\,r - \nabla\cdot\vec{\vec{\tau}} \tag{18}$$

where the density of mixture $\overline{\rho_m}$, ρ_m and $\tilde{\rho_m}$ are:

- Homogeneous model: $\overline{\rho_m} = \rho_1\,\lambda_1 + \rho_2\,\lambda_2$

- Conventional: $= \rho_m = \rho_1\,\alpha_1 + \rho_2\,\alpha_2$
- $\tilde{\rho_m} = \rho_1\,\lambda_1\,\frac{\lambda_1}{\alpha_1} + \rho_2\,\lambda_2\,\frac{\lambda_2}{\alpha_2}$

- **Viscous Stress Tensor Modeling**

The term $\nabla\cdot\vec{\vec{\tau}}$ is related to surface forces due to the stresses on the sides of the control surface. In polar coordinates considering radial and azimuthal direction, the Gauss theorem in limited form is applied in the stress tensor.

$$\int_{A_k(z,t)} \nabla\cdot\vec{\vec{\tau}}\,dA = \frac{\partial}{\partial r}\int_{A_k(r,t)} \vec{\vec{\tau}}\cdot\vec{n}_r\,dA + \oint_{\xi(r,t)+\xi_k(r,t)} \vec{n}_k\cdot\vec{\vec{\tau}}\,\frac{d\xi}{\vec{n}_k\cdot\vec{n}_{k\xi}} \tag{19}$$

where vector $\vec{n}_k$ is normal to interface pointed outside of face k. Unitary vector $\vec{n}_{k\xi}$ is normal to ξ in the plane A_k. The term ξ_k is the contact of the interface to the wall. ξ is the interface of the fluids.

For simplification, the channel of the impeller was considered as a duct and the cross-section area is represented by the hydraulic diameter. The mixture flow is considered homogeneous and thus density and viscosity are calculate with this premise.

Eq. 19 is developed in Appendix A, section *Viscous Stress Tensor Modeling*. The resulting terms in radial direction are used in Eq. 18. Summarizing the results for the first term on the right hand side of Eq. 19 for radial and azimuthal direction are, respectively from Appendix A:

$$\int_{A_k(r,t)} \frac{\partial}{\partial r}\left(\vec{\vec{\tau}}\cdot\vec{n}_r\right)dA\Big|_r = 4\,\mu\frac{\lambda_k}{\alpha_k}\frac{Q_m}{2\,\pi\,h}\frac{1}{r^3} \tag{91}$$

$$\int_{A_k(r,t)} \frac{\partial}{\partial r}\left(\vec{\vec{\tau}}\cdot\vec{n}_r\right)dA\Big|_\theta = -4\,\mu\frac{\lambda_k}{\alpha_k}\frac{Q_m}{2\,\pi\,h}\frac{1}{r^3}\,\cot\beta \tag{92}$$

The last term on the right hand side of Eq. 19 for radial and azimuthal direction becomes:

$$\begin{aligned}\hat{r} &:= \frac{f}{8}\,\rho_m\,\frac{j_m(r)^2}{\sin\beta}\,2\left(\frac{1}{h}+\frac{Z_b}{2\,\pi\,r}\right)\\ \hat{\theta} &:= -\frac{f}{4}\,\rho_m\,\frac{j_m(r)^2}{\sin\beta}\,\cot\beta\left(\frac{1}{h}+\frac{Z_b}{2\,\pi\,r}\right)\end{aligned} \tag{102}$$

The terms are dependent on the friction factor, mixture flow rate, and geometry of the impeller.

- **Radial pressure**

In order to expand the model for use in other pumps, dimensionless numbers were used. So, Eq. 18 is developed in Appendix A, in section *Radial and viscous term*. Some terms can be grouped in G_1, G_2, G_3 and G_4. They have all geometric constants, the only exception is the friction factor, f. So, summarizing:

- Dimensionless group for two-phase head: $C_H = \Delta P/(\overline{\rho_m}\,\omega^2\,r_o^2)$
- Dimensionless group for two-phase flow rate: $C_Q = Q_m/(\omega\,r_o^3)$

These two terms C_Q and C_H are very common to represent the ESP performance (Estevam, 2002 [4]; Gamboa, 2009 [11]; Monte Verde et al., 2017 [12]).

The first geometric coefficient G_1 have *Factor 1* which is always higher than one because $r_o > r_i$. *Factor 2* follows the same logic, $r_o > h$, so it is higher than one. Thus, the result of the geometric constant G_1 is higher than zero.

Another important term is the *Factor 3* which is a result of the viscous stress tensor when it is integrated in relation to r. This term is positive because it is related to the subtraction between radius, so it is higher than zero. The terms G_2, G_3 and G_4, as shown below, are higher than zero. The term G_2 is related to fluid properties, such as the viscosity that has been divided by the mixture density ρ_m, resulting in a value almost zero. When the viscosity increases due to changes in the fluid properties (temperature, heavy oils, among others), this term increases.

- Geometric coefficients:
  - Factor 1: $r_o/r_i = f_1 \quad \rightarrow \quad > 1$
  - Factor 2: $r_o/h = f_2 \quad \rightarrow \quad > 1$
  - Factor 3: $\left[\frac{1}{h}\left(\frac{1}{r_i} - \frac{1}{r_o}\right) + \frac{Z_b}{4\pi}\left(\frac{1}{r_i^2} - \frac{1}{r_o^2}\right)\right] = f_3 \quad \rightarrow \quad > 0$
  - Geometric constant 1: $G_1 = \left[\frac{(1+\cot^2\beta)}{8\pi^2}\right] f_2^2 (f_1^2 - 1) \quad \rightarrow \quad > 0$
  - Geometric constant 2: $G_2 = \left[\left(\frac{\cot\beta}{\pi}\right) f_2 \ln f_1\right] + \frac{\mu}{\rho_m}\frac{\lambda_k}{\alpha_k}\frac{1}{\omega\pi h r_o}\left[\left(\frac{r_o}{r_i}\right)^2 - 1\right] \quad \rightarrow \quad > 0$
  - Geometric constant 3: $G_3 = \frac{1}{2}\left[1 - \left(\frac{1}{f_1}\right)^2\right] \quad \rightarrow \quad > 0$
  - Geometric constant 4: $G_4 = \frac{r_o^4}{4\pi^2 h^2}\frac{1}{\sin\beta} f_3 \quad \rightarrow \quad > 0$

The dimensionless Eq. 20 was acquired dividing Eq. 18 by $\overline{\rho_m}\,\omega^2\, r_o^2$. After that, the resultant equation was simplified as it was used with air and water (or gas/liquid) and the difference between their densities is higher, so the term $\rho_m/\overline{\rho_m} \approx \alpha_1/\lambda_1$ and $\tilde{\rho_m}/\overline{\rho_m} \approx \lambda_1/\alpha_1$ were simplified. The complete passages between equations were written in the supplementary material, in Appendix A in the item *Radial pressure* and the result is showed in Table 3.

TABLE 3 Model dimensionless equation.

Variable	Equation
C_H	$= B_3\, G_3 - B_2\, C_Q + B_1\, C_Q^2$ (20)
B_1	$= \left(\frac{\lambda_1}{\alpha_1}\, G_1 - \frac{\alpha_1}{\lambda_1}\, G_4\, \frac{f}{4}\right)$
B_2	$= G_2$
B_3	$= \frac{1}{2}\left(\frac{\alpha_1}{\lambda_1}\right)$

The coefficients of Eq. 20 is adjusted in accordance with the experimental data acquired. Figure 11 shows the plot for experimental data of C_H x C_Q. In the chart, the symbol x in red indicates the point where the surging is occurring, the symbol indicated by the blue circles is a stable region for the pump operation. The geometric interpretation follows a quadratic equation: the term $(\alpha_1/\lambda_1\, G_4\, f/4) > (\lambda_1/\alpha_1\, G_1)$ meaning that B_1 is negative and the parabola opens downward. Besides, the y-intercept is located at the point (0, B_3).

The gas void fraction α_k is a variable difficult to measure. It was calculated using the drift-flux model described in the next sections. The experimental data used in Fig. 11(a) has an R-squared equal to 0.95 which indicates a good fidelity with reality. The coefficients for the adjusted model, black line in Fig. 11(a), are: $B_1 = -214.48$, $B_2 = 22.41$ and $B_3 = -0.27$.

The friction factor f can be calculated with the coefficient B_1. When f is calculated using the model, it is referred as f_{model}. For comparison, as the study comprises the friction factor calculated inside an impeller and all complications

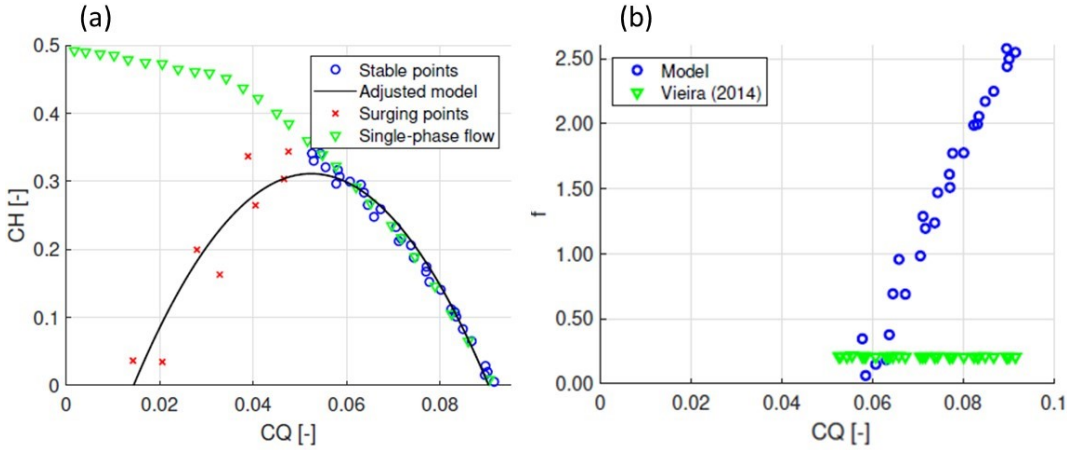

FIGURE 11 (a) Adjusted model plotted in relation to dimensionless numbers, C_H and C_Q - (b) Friction factor: model x Vieira (2014) [13].

that it brings to the study, Vieira (2014) [13] calculated it using some correlations. The friction factor was calculated using the correlations showed in Appendix A, in section *Friction Factor Comparison*, and it was denoted as $f_{r\beta\omega}$. So, $f_{r\beta\omega}$ is equal to:

$$f_{r\beta\omega} = \bar{F}_r \cdot \bar{F}_\beta \cdot \bar{F}_\omega \cdot \bar{f} \quad \rightarrow \quad f_{r\beta\omega} = 0.2079 \tag{21}$$

where $\bar{F}_r = 1.2420$, $\bar{F}_\beta = 1.1614$, $\bar{F}_\omega = 1.4619$ and $\bar{f} = 0.0986$. They were related to the corrections done for turbulent flow, channel curvature and pump rotation, respectively. The value of $\bar{f}$ is calculated by the Churchill correlation (Churchill, 1977 [25]). Considering these corrections made for the centrifugal pump, the result of friction factor is $f_{r\beta\omega} = 0.2079$, representing 210% higher than the one predicted for a pipe flow.

The mean value of $\bar{f}$ corresponds to the value a little higher than the expected value using the Moody diagram shown in Fig. 17. For the present problem the two-phase mixture Reynolds number is calculated by $Re = \rho_m j_{ms} D_h/\mu_m$. The friction factor expected for an average Reynolds (Re) of 13375 is between 0.025 to 0.080 as showed by the red line in the Moody diagram in Fig. 17 in Appendix B.

The friction factor calculated using the model f_{model} is compared with Vieira, 2014 [13], and it is shown in Fig. 11(b) represented by the blue circles. It is observed that there is no variation of the friction factor calculated by Vieira even with the increase of the flow rate (C_Q). However for values near the BEP the friction factors are of the same magnitude.

In a real situation, the flow conditions inside an ESP vary when the flow rate changes. Some studies related that when the ratio between Q/Q_{BEP} is higher than one, the flow direction tends to point to the suction blade side, increasing the shock losses in this region. Besides, the vortices form in the pressure blade side, in the counter-clockwise direction. On the other hand, when the ratio Q/Q_{BEP} is lower than one, the flow direction tends to shock with the pressure blade side. In this situation, the vortices form in the suction blade side, rotating in a clockwise direction (Feng et al., 2010 [1]).

Therefore, the friction factor calculated using the model tends to reduce as the flow rate C_Q approximates to the

BEP, which is in agreement with the literature because the losses reduce. However, the value of f_{model} moving away from the BEP increase so much that reaches values not expected from friction factor, such as 2.44 at $C_Q = 0.089$. This value is overrated because all losses are included in the f_{model}, such as shock losses, recirculating flows, among others. This is a result of one premise adopted: flow parallel to the blade.

Deeply studies should be realized for the friction factor inside an ESP operating under two-phase flow conditions. The phenomenon sustains many variables that may impact the calculus of friction factor, such as the Reynolds number.

3.3 | Momentum Transfer Between Phases

In this section, the rate of momentum transfer per unit volume of liquid phase to the gas phase is estimated in radial direction. It will be used to get the radial slip which will be projected tangentially to the blades. Therefore, different from what was done in the former section, where the goal was the pressure gradient, the next step wants to eliminate this term. To achieve this, the equations of momentum for both phases will be subtracted in radial direction and the term M_{2r} will be estimated. The equations in radial direction for phases 1 and 2 are discussed in the next steps.

- **Radial direction (polar) $\hat{r}$:**

$$\alpha_k \rho_k \left(v_{kr} \frac{\partial}{\partial r} v_{kr} + \frac{v_{k\theta}}{r} \frac{\partial}{\partial \theta} v_{kr} - \frac{v_{k\theta}^2}{r} \right) = -\alpha_k \frac{\partial}{\partial r} p_k + \alpha_k \rho_k g_r - M_{kr} + S_{kr} + \nabla \cdot \vec{\vec{\tau}} \tag{22}$$

The pressure is considered equal for both phases ($p_1 = p_2$), the gravity was neglected by hypothesis and, the velocity field was simplified, depending on the radius variation, which means that $\partial / \partial \theta = 0$. The momentum transferred by one phase is received by the other, this means that $M_{1r} = -M_{2r}$. The development after applying these simplifications is in Appendix A, in the section *Momentum Transfer Between Phases*. The resultant equation is:

$$\frac{M_{2r}}{\alpha_1 \alpha_2} = \widetilde{\Delta\rho} \left[\frac{(1 + \cot^2 \beta)}{4\pi^2 h^2} \right] Q_m^2 \left(\frac{-1}{r^3} \right) + \overline{\Delta\rho} \left(\frac{\cot \beta}{\pi h} \right) \omega \, Q_m \left(\frac{1}{r} \right) - \Delta\rho \, \omega^2 \, r - \langle \nabla \cdot \vec{\vec{\tau}} \rangle \tag{23}$$

The terms involved with density are:

$$\circ \quad \Delta\rho = \rho_1 - \rho_2 \qquad \circ \quad \overline{\Delta\rho} = \rho_1 \left(\frac{\lambda_1}{\alpha_1} \right) - \rho_2 \left(\frac{\lambda_2}{\alpha_2} \right) \qquad \circ \quad \widetilde{\Delta\rho} = \rho_1 \left(\frac{\lambda_1}{\alpha_1} \right)^2 - \rho_2 \left(\frac{\lambda_2}{\alpha_2} \right)^2 \tag{24}$$

In the classic models, generally the drag is considered because the relative velocity appears from this term. This force is predominant in stationary and developed flows, such as ducts in steady state without convective terms. This is not the case in this study where the impeller has a strong convective acceleration. Therefore, the pseudo forces are important and should all be considered, including Basset and virtual mass forces. The interfacial term is defined using the Zuber model (Zuber, 1964 [26], Ishii and Hibiki, 2010 [24]). Thus, M_{2r} is given by:

$$M_{2r} = -\frac{\alpha_2}{B_b} \left(\sum \vec{F}_{R\ bubbles} \right) \qquad \text{and} \qquad \sum \vec{F}_{R\ bubbles} = \vec{F}_D + \vec{F}_V + \vec{F}_B \tag{25}$$

where α_2 is the gas fraction, B_b is the mean volume of a bubble, and $\sum \vec{F}_{R\ bubbles}$ is the mean resultant force in one bubble. The mean volume of a bubble will be approximated by the volume of a sphere, given by: $B_b = 4\pi r_b^3/3$, where r_b is the bubble radius. The drag force is $\vec{F}_D$, the virtual mass force is $\vec{F}_V$ and Basset force is $\vec{F}_B$.

The forces for a bubble with an average diameter in the flow with radius r_b are discussed in Appendix A, in the section *Momentum Transfer Between Phases*. Each term showed were developed in the same section. The results are shown here. Therefore each force provide the terms (Ishii and Hibiki, 2010):

- $\vec{M}_{2r}^{D} = \alpha\,\rho_1\,C_A\,\vec{v}_{sr}\,||\vec{v}_s||$ where $C_A = \frac{3\,C_D}{8\,r_b}$
- $M_2^V = \alpha\,\rho_1\,C_V\,(v_2\cdot\nabla v_2 - v_1\cdot\nabla v_1)$
- $\vec{M}_2^B = \alpha\,\rho_1\,C_B\,(\vec{v}_2\cdot\nabla\vec{v}_2 - \vec{v}_1\cdot\nabla\vec{v}_1)$ and $C_B = \frac{9}{r_b}\sqrt{\frac{\mu_m\,t}{\pi\,\rho_1}}$

where the term C_D indicates the drag coefficient and the density considered inside the drag force is related to the continuous phase. The term C_V is the virtual mass coefficient and it is approximate to $1/2$. At last, the term C_B indicates the Basset coefficient. So, considering all these terms:

$$M_{2r} = \alpha\,\rho_1\,C_A\,\sin\beta\,v_{s,s}\,||\vec{v}_s|| + \alpha\,\rho_1\,(C_B + C_V)\left[\left(\frac{\lambda_2}{\alpha_2}\right)^2 - \left(\frac{\lambda_1}{\alpha_1}\right)^2\right]\left[\frac{(1+\cot^2\beta)}{4\,\pi^2\,h^2}\right]Q_m^2\left(\frac{-1}{r^3}\right) \tag{26}$$

Finally, Eq. 23 and 26 are placed together and the entire development is done in Appendix A, in section *Development of interfacial terms*. The slip velocity was isolated in the main direction of the flow ($\hat{s}$), $v_{s,s}$ resulting in Eq. 162. The coefficients ΔC^∞ and C_A^∞ are considered for an isolate bubble and they are indicated with superscript ∞. They are:

$$\Delta C^\infty = \frac{C_B + C_V}{1-\alpha} \qquad C_A^\infty = \frac{C_A}{1-\alpha}$$

Therefore the format of the model is rewritten from Eq. 162:

$$-\overline{v_{s,s}}^{\,2} = -A_1\,Q_m^2 + A_2\,\omega Q_m - A_3\,\omega^2 \tag{27}$$

where $v_{s,s}$, Q_m and ω are, respectively, the slip velocity in the $\hat{s}$-direction, mixture flow rate and rotational speed. The terms in Eq. 27 are showed in Table 4.

TABLE 4 Variables in Eq. 27.

Variable	Equation
A_1	$= \frac{1}{4\,C_A^\infty\,\pi^2\,h^2}\left\{\left[\frac{\widetilde{\Delta\rho}}{\rho_1} - \Delta C^\infty\,Lambdas\right]\left(\frac{\csc^2\beta}{\sin\beta}\right)\frac{1}{r_i^2\,r_o^2} - \frac{\rho_m}{\rho_1}\,\frac{f}{4}\left[\left(\frac{1}{\sin^2\beta}\right)\frac{f_3}{\Delta r}\right]\right\}$
$Lambdas$	$= \left[\left(\frac{\lambda_2}{\alpha_2}\right)^2 - \left(\frac{\lambda_1}{\alpha_1}\right)^2\right]$
A_2	$= \frac{\overline{\Delta\rho}}{\rho_1}\left(\frac{\cot\beta}{\sin\beta}\right)\frac{\ln(r_o/r_i)}{C_A^\infty\,\pi\,h\,\Delta r} + 2\,\frac{\mu}{\rho_1}\,\frac{1}{C_A^\infty}\,\frac{1}{\pi\,h\,\sin\beta}\,\frac{\lambda_k}{\alpha_k}\left(\frac{\bar{r}}{r_o^2\,r_i^2}\right)\frac{1}{\omega}$
A_3	$= \frac{1}{C_A^\infty\,\sin\beta}\left(\frac{\Delta\rho}{\rho_1}\right)\bar{r}$
C_A^∞	$= \left(\frac{3\,C_D}{8 r_b}\right)\frac{1}{1-\alpha}$
ΔC^∞	$= C_B^\infty + C_V^\infty = \left(\frac{9}{r_b}\sqrt{\frac{\mu_m\,t}{\pi\,\rho_1}} + \frac{1}{2}\right)\frac{1}{1-\alpha}$

The coefficients $A_{k,k=\{1,2,3\}}$ depend on λ, α, ΔC^∞ and C_A^∞. In the bubble flow pattern there is a chance that the

terms ΔC^{∞} and C_A^{∞} can be practically constant and $\lambda/\alpha \sim 1$. This means that those coefficients do not depend mostly on λ/α so do not change so much compared to the others. So, the drift-flux model becomes:

$$\overline{v_{2s}} = \left(\frac{\lambda_2}{\alpha_2}\right)\left[\left(\frac{Q_m}{2\,\pi\,h}\right)\frac{\ln\left(r_o/r_i\right)}{\left(r_o - r_i\right)}\,\frac{1}{\sin\beta}\right] = C_0\left(\frac{Q_m}{2\,\pi\,h}\right)\frac{\ln\left(r_o/r_i\right)}{\left(r_o - r_i\right)}\,\frac{1}{\sin\beta} + (1-\alpha)\overline{v_{s,s}} \tag{28}$$

- **Dimensionless:**

To generalize the model, it has to be dimensionless. So, Eq. 27 was divided by $(\Delta\rho/\rho_1)\,\omega^2\,r_o^2$. The Froude number for two-phase flow $Fr_{TP,s}$ for the slip under a centrifugal field and the mixture Froude number Fr_m are given by:

$$Fr_{TP,s}^2 = \frac{\rho_1\,\overline{v_{s,s}}^2}{\Delta\rho\,\omega^2\,r_o^2} \qquad \text{and} \qquad Fr_m = \sqrt{\frac{\rho_1}{\Delta\rho}}\left(\frac{Q_m}{2\,\pi\,r_o\,h}\right)\Big/\omega r_o$$

Using both Froude numbers in Eq. 27, the dimensionless model format is rewritten as:

$$Fr_{TP,s}^2 = A_1^{'}\,Fr_m^2 - A_2^{'}Fr_m + A_3^{'} \tag{29}$$

where $A_{k,k=\{1,2,3\}}^{'} = f\left(\lambda, \alpha, C_A^{\infty}, \Delta C^{\infty}\right)$

$$\begin{aligned}
&\circ\quad A_1^{'} = \frac{1}{C_A^{\infty}}\left\{\left[\frac{\widetilde{\Delta\rho}}{\rho_1} - \Delta C^{\infty}\,Lambdas\right]\left(\frac{\csc^2\beta}{\sin\beta}\right)\frac{1}{r_i^2\,r_o^2} - \frac{\rho_m}{\rho_1}\,\frac{f}{4}\left[\left(\frac{r_o^2}{\sin^2\beta}\right)\frac{f_3}{\Delta r}\right]\right\}\\
&\circ\quad A_2^{'} = 2\left(\frac{\overline{\Delta\rho}}{\sqrt{\Delta\rho\,\rho_1}}\right)\left(\frac{\cot\beta}{\sin\beta}\right)\frac{\ln(r_o/r_i)}{C_A^{\infty}\left(r_o - r_i\right)}\\
&\circ\quad A_3^{'} = \frac{\bar{r}}{r_o^2\,C_A^{\infty}\,\sin\beta}
\end{aligned} \tag{30}$$

Figure 12 shows the result of Eq. 29. The mixture Froude number and the two-phase Froude number increase together until the mixture Froude number equals 0.035. From this point, the two-phase Froude number begins to decrease, and the mixture Froude number, to increase. In the experiments, this is the region where the energy delivered to the fluid is decreasing due to many bubbles present in the flow, forming a swarm in the impeller channel. This was predicted by Gamboa (2009) [11] and Monte Verde et al. (2017) [12], who proposed that the flow pattern in this region is the gas pocket pattern. In a situation where the slip velocity is close to zero, $v_s \rightarrow 0$, the proposed model becomes the homogeneous model.

Unfortunately, the data obtained by the image post-processing did not reach this region because the gas phase was distorted, not showing as bubbles. The gas velocity was not measured in this region. However, this region is influenced by four variables, $A_k^{'}$ in Eq. 29. The coefficients are calculated using the method of non linear least square, providing R^2 equals to 0.99. The fit used the experimental data to calculate the coefficients. The term C_A^{∞} is present in $A_2^{'}$ and $A_3^{'}$ and is the easiest to acquire. On the other hand, the term $A_1^{'}$ is influenced by λ, α and ΔC^{∞}. These four variables are discussed in the section *Model results*. The coefficients in Eq. 29 are: $A_1^{'} = 6.971$, $A_2^{'} = 0.501$ and $A_3^{'} = 0.114$.

The mean value of mixture volumetric flux in $\hat{r}$ and $\hat{s}$ direction are:

$$j_{mr} = \left(\frac{Q_m}{2\,\pi\,h}\right)\frac{\ln\left(r_o/r_i\right)}{\left(r_o - r_i\right)} \qquad \text{and} \qquad j_{ms} = j_{mr}\,\frac{1}{\sin\beta} \tag{31}$$

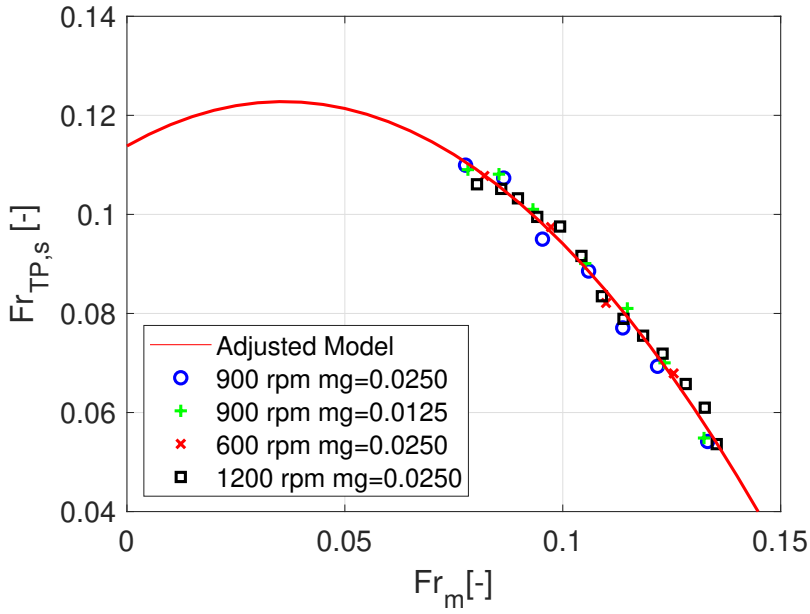

FIGURE 12 Adjusted model using Dimensionless numbers: $Fr_{TP,s}$ x Fr_m.

Eq. 13 was multiplied by the term $\sqrt{\rho_1/\Delta\rho}\cdot 1/\omega\, r_o$ and the terms in Eq. 31 were used. After that, we may define:

$$Fr_{2,s} = \sqrt{\frac{\rho_1}{\Delta\rho}}\cdot\frac{v_{2s}}{\omega\, r_o} \qquad \text{and} \qquad C_0^{'} = C_0\left[\frac{r_o\,\ln(r_o/r_i)}{\sin\beta\,(r_o - r_i)}\right]$$

These terms $Fr_{2,s}$, $C_0^{'}$, $Fr_{TP,s}$ and Fr_m are used in Eq. 13 and results in:

$$Fr_{2,s} = C_0^{'} Fr_m + (1-\alpha)\, Fr_{TP,s} \tag{32}$$

Using Eq. 29 in Eq. 32 and considering the liquid phase faster than the gas phase ($v_1 > v_2$), the term $v_{s,s}^2$ should be negative. Due to this, as this term is squared, Eq. 32 is corrected changing the signal of the drift-flux velocity in its dimensionless form. Considering this, Eq. 32 becomes:

$$Fr_{2,s} = C_0^{'} Fr_m - (1-\alpha)\sqrt{A_1^{'}\, Fr_m^2 - A_2^{'}\, Fr_m + A_3^{'}} \tag{33}$$

The coefficients presented in Eq. 33 were calculated using the non-linear least square method, which provides R^2 equals to 0.86. The terms $A_k^{'}$ are under a square root, which means that this expression suffers about the loss of the signal's information. This is one of the factors that influence the value of R^2 if we compare it with Eq. 29, which tends to be lesser. The distribution coefficient of C_0 is equal to 1.23.

3.4 | Transition Criteria for Surging and Gas Locking

The transition criteria propose a method to predict the surging and gas locking conditions. First, the forces on the bubble are discussed in appendix A, in section *Development of Bubble Forces* to predict the bubble direction in the impeller channel, even its stagnation. So, summarizing the forces in Table 5.

TABLE 5 Forces considered in bubble.

Force	Equation
Drag	$\overline{F_{2s}^{D}} = \frac{1}{2} A_p \, C_D \, \rho_1 \, \overline{v_{s,s}}^2$
Basset and Added Mass	$\overline{F_{2r}^{VB}} = -\rho_1 \, B_b \, \Delta C \, Lambdas \, \csc^2 \beta \left[\frac{-\bar{r}}{r_i^2 \, r_o^2} \right] \left(\frac{Q_m}{2\pi \, h} \right)^2$
Fictitious (Centripetal and Coriolis)	$\vec{F}_{2r}^{F} = -m_g \left[2\omega \, \frac{\lambda_2}{\alpha_2} \, \cot\beta \left(\frac{Q_m}{2\,\pi\,h} \right) \frac{\ln(r_o/r_i)}{\Delta r} - \omega^2 \, \frac{(r_o^2 - r_i^2)}{2\Delta r} \right]$ $\vec{F}_{2\theta}^{F} = -m_g \left[2\omega \, \frac{\lambda_2}{\alpha_2} \left(\frac{Q_m}{2\,\pi\,h} \right) \frac{\ln(r_o/r_i)}{\Delta r} \right]$
Buoyancy	$\overline{F_r^E} = -B_b \left\{ \tilde{\rho}_m \left[\frac{(1+\cot^2\beta)}{4\,\pi^2\,h^2} \right] Q_m^2 \frac{1}{\Delta r} \left[\frac{1}{2} \frac{(r_i^2 - r_o^2)}{r_i^2 \, r_o^2} \right] + \overline{\rho_m} \left(\frac{\cot\beta}{\pi\,h} \right) \omega \, \frac{Q_m}{\Delta r} \, \ln \frac{r_o}{r_i} \right.$ $\left. -\rho_m \, \omega^2 \, \frac{(r_o^2 - r_i^2)}{2\,\Delta r} - \mu \frac{\lambda_k}{\alpha_k} \frac{Q_m}{\pi\,h} \frac{1}{\Delta r} \left(\frac{r_o^2 - r_i^2}{r_i^2 \, r_o^2} \right) - \frac{f}{4} \frac{\rho_m}{\sin\beta} \left(\frac{Q_m}{2\,\pi\,h} \right)^2 \frac{f_3}{\Delta r} \right\}$ $\overline{F_\theta^E} = -B_b \left\{ \widetilde{\rho_m} \, 2 \, \cot\beta \left(\frac{Q_m}{2\pi h} \right)^2 \left[\left(\frac{\bar{r}}{r_i^2 \, r_o^2} \right) \right] + 2\,\overline{\rho_m} \, \omega \left(\frac{Q_m}{2\,\pi\,h} \right) \frac{\ln(r_o/r_i)}{\Delta r} \right.$ $\left. -2\,\mu \frac{\lambda_k}{\alpha_k} \frac{Q_m}{\pi\,h} \, \cot\beta \left(\frac{\bar{r}}{r_i^2 \, r_o^2} \right) + \frac{f}{4} \rho_m \frac{\cot\beta}{\sin\beta} \left(\frac{Q_m}{2\,\pi\,h} \right)^2 \frac{f_3}{\Delta r} \right\}$

The subscripts r and θ indicates the forces in polar coordinates. In possess of these forces, the criteria conditions are established in the following section.

3.4.1 | Criteria Conditions

The criteria used here are an extension of those proposed for ducts and applied for centrifugal pumps by some authors (Murakami and Minemura, 1974 [9], Estevam, 2002 [4], Barrios, 2007 [5], among others). Visually, the surging occurs when the bubbles start to coalesce.

From the Transition Criteria, the bubble is expected to follow a path in the suction side when the sum of the forces in the $\hat{n}$ direction is positive, or it can go to the pressure side when the opposite happens. This might take place when the resulting force in the normal $\hat{n}$ direction begins to be higher than the resulting force in the longitudinal direction, which is $\hat{s}$.

The criteria are expected to indicate the region where the surging and gas locking begins. As the water flow rate begins to decrease, the gas ratio increases, thus the bubble swarms appear in the impeller channel, characterizing the flow pattern as gas pocket. Once the ratio of gas still increases and reaches a segregated flow pattern, the gas locking is established, ceasing the pump operation.

Therefore the criteria starts with the idea that the beginning of the surging or gas locking occurs when forces in both directions ($\hat{n}$ $\hat{s}$) are equal in modulus.

$$\sum |\vec{F}_{R\ bubbles,s}| = \sum |\vec{F}_{R\ bubbles,n}| \tag{34}$$

Next, Eq. 34 will be developed for Conditions 1 and 2.

Condition 1

The first condition tested is the point where the longitudinal force in $\hat{s}$ is equal to the transversal force in $\hat{n}$. This corresponds to the threshold condition, as the forces are equal in modulus. This condition considers $F_s = F_n$. So, from Eq. 34:

$$\overline{\vec{F}_{2s}^{D}} + \overline{\vec{F}_{2s}^{VB}} + \overline{\vec{F}_{2s}^{E}} + \overline{\vec{F}_{2s}^{F}} + \overline{\vec{F}_{2n}^{VB}} + \overline{\vec{F}_{2n}^{E}} + \overline{\vec{F}_{2n}^{F}} = 0 \tag{35}$$

The development of Eq. 35 is presented in Appendix A, in section *Development of Transition Criteria*. The result is Eq. 36.

$$C_H = D_1 C_Q^2 + D_2 C_Q + \left(D_3 F r_{TP,s}^2 + D_4\right) \tag{36}$$

where $D'_{k,k=\{1,2,3,4\}} = f(\lambda, C_D, \Delta C)$

$$\begin{aligned}
\circ \quad D_1 &= \frac{\rho_1}{\overline{\overline{\rho_m}}}\,\Delta C\, Lambdas\, G_1 + \frac{\widetilde{\overline{\rho_m}}}{\overline{\overline{\rho_m}}}\frac{\cot\beta}{4\pi^2}\left(\frac{r_o}{h}\right)^2\left[\left(\frac{r_o}{r_i}\right)^2 - 1\right] G_5 + \frac{f}{4}\frac{\rho_m}{\overline{\overline{\rho_m}}}\frac{\cot\beta}{\sin\beta}\, G_5\left(\frac{r_o^4}{4\,\pi^2\,h^2}\right) f_3 \\
\circ \quad D_2 &= \frac{\rho_2}{\overline{\overline{\rho_m}}}\frac{\lambda_2}{\alpha_2}\left(\frac{r_o}{h}\right)\frac{\ln(r_o/r_i)}{\pi}\, G_5 - \frac{\rho_2}{\overline{\overline{\rho_m}}}\frac{\lambda_2}{\alpha_2}\cot\beta\left(\frac{r_o}{h}\right)\frac{\ln(r_o/r_i)}{\pi} \\
&\quad - \left(\frac{r_o}{h}\right)\frac{\ln(r_o/r_i)}{\pi}\, G_5 + \frac{\mu}{\overline{\overline{\rho_m}}}\frac{\lambda_k}{\alpha_k}\frac{\cot\beta}{(\omega\,\pi\,h)}\frac{1}{r_o}\left[\left(\frac{r_o}{r_i}\right)^2 - 1\right] G_5 \\
\circ \quad D_3 &= \frac{1}{2}\left(\frac{A_p}{B_b}\right)\frac{C_D\,\Delta r}{(\sin\beta + \cos\beta)}\,\frac{\Delta\rho}{\overline{\overline{\rho_m}}} \\
\circ \quad D_4 &= \frac{\rho_2}{\overline{\overline{\rho_m}}}\,\frac{1}{2}\left[1 - \left(\frac{r_i}{r_o}\right)^2\right]
\end{aligned} \tag{37}$$

Condition 2

The second condition is almost the same as the first. However, as the forces are equal in modulus, here is the point where longitudinal force in $\hat{s}$ is equal to the transversal force in $\hat{n}$ by the other way. This means that $F_s = -F_n$. So, from Eq. 34:

$$\overline{\vec{F}_{2s}^{D}} + \overline{\vec{F}_{2s}^{VB}} + \overline{\vec{F}_{2s}^{E}} + \overline{\vec{F}_{2s}^{F}} - \overline{\vec{F}_{2n}^{VB}} - \overline{\vec{F}_{2n}^{E}} - \overline{\vec{F}_{2n}^{F}} = 0 \tag{38}$$

The development of Eq. 38 is presented in Appendix A, in the section *Development of Transition Criteria*. The result is Eq. 39.

$$C_H = E_1 C_Q^2 + E_2 C_Q + \left(E_3 F r_{TP,s}^2 + D_4\right) \tag{39}$$

where $E'_{k,k=\{1,2,3\}} = f(\lambda, C_D, \Delta C)$

$$\begin{aligned}
\circ \quad E_1 &= \frac{\rho_1}{\overline{\overline{\rho_m}}}\,\Delta C\, Lambdas\, G_1 + \frac{\widetilde{\overline{\rho_m}}}{\overline{\overline{\rho_m}}}\frac{\cot\beta}{4\pi^2}\left(\frac{r_o}{h}\right)^2\left[\left(\frac{r_o}{r_i}\right)^2 - 1\right] G_6 + \frac{f}{4}\frac{\rho_m}{\overline{\overline{\rho_m}}}\frac{\cot\beta}{\sin\beta}\, G_6\left(\frac{r_o^4}{4\,\pi^2\,h^2}\right) f_3 \\
\circ \quad E_2 &= \frac{\rho_2}{\overline{\overline{\rho_m}}}\frac{\lambda_2}{\alpha_2}\left(\frac{r_o}{h}\right)\frac{\ln(r_o/r_i)}{\pi}\, G_6 - \frac{\rho_2}{\overline{\overline{\rho_m}}}\frac{\lambda_2}{\alpha_2}\cot\beta\left(\frac{r_o}{h}\right)\frac{\ln(r_o/r_i)}{\pi}
\end{aligned}$$

$$- \left(\frac{r_o}{h}\right) \frac{\ln(r_o/r_i)}{\pi} G_6 + \frac{\mu}{\overline{\rho_m}} \frac{\lambda_k}{\alpha_k} \frac{\cot\beta}{(\omega\,\pi\,h)} \frac{1}{r_o} \left[\left(\frac{r_o}{r_i}\right)^2 - 1\right] G_6$$

$$\circ \quad E_3 = \frac{1}{2} \left(\frac{A_p}{B_b}\right) \frac{C_D\,\Delta r}{(\sin\beta - \cos\beta)} \frac{\Delta\rho}{\overline{\rho_m}} \tag{40}$$

Figure 13 shows the chart with both conditions plotted. The red curve indicates the condition 1 and the blue curve, condition 2. When the blue curve encounters the experimental curve (experimental points or black line - model), this indicates the point where surging begins.

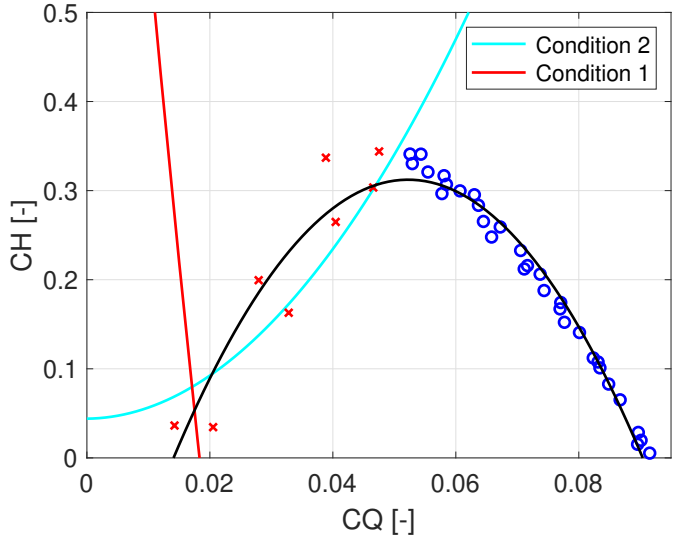

FIGURE 13 Pump curve and Transition criteria - Condition 1 (red line) and Condition 2 (blue line).

The coalescence raises changing the balance on bubble forces resulting in the phenomenon knowing as surging. This is what happens in condition two. As the ratio of gas keeps increasing in the impeller channels, the coalescence increases and the bubble movement reduces until it stops, leading into gas-locking condition. This region is shown by the encounter of both curves (red and blue ones). At this point, the resultant of forces is equal to zero.

The gas locking occurs when the mixture flow rate Q_m decreases until the pump was unable to transfer energy to the fluid, so the pressure increment is null. When this occurs, the forces acting on bubbles stabilizes, rendering the air being unable to move. Thus it promotes the gas locking in the pump.

4 | MODEL RESULTS AND DISCUSSION

The results of the distribution parameter C_0, the Basset and Added Mass coefficients, the bubble shape and general discussion about the model are showed in this section.

4.1 | Distribution Parameter

Wallis (1969) [27] pointed out that for a vertical dispersed flow, the distribution parameter lies between 1.0 and 1.5 being more likely 1.2. However, for a horizontal and near-horizontal flow, as the bubbles tend to accumulate at the top of the pipe, it is commonly assumed that they move at the average mixture velocity, hence the flow distribution parameter is equal to one.

Clark and Flemmer (1985) [28] performed an experimental study to improve the understanding of upward/downward vertical flows. Their average values for C_0 in upward flow was 1.07 and in downward flow, 1.17. The authors proposed a correlation to obtain the distribution parameter as a function of void fraction for each flow direction, which are:

$$\begin{aligned} C_0 &= 0.934\,(1 + 1.42\alpha) \quad \rightarrow \quad \text{Upward vertical flow} \\ C_0 &= 1.521\,(1 - 3.67\alpha) \quad \rightarrow \quad \text{Downward vertical flow} \end{aligned} \tag{41}$$

Takashi and Ishii (2002) [29] proposed a relation using the density of the phases, considering the effect of bubble size on the phase distribution, since the presence of bubbles govern the distribution of the void fraction. Indirectly, the authors associates the Sauter mean diameter, d_{Sm}, with the void fraction. In addition, Eq. 42 have its coefficient (−22) approximated by the least-squares method.

$$C_0 = \left(1.2 - 0.2\sqrt{\rho_2/\rho_1}\right)\left[1 - exp(-22\langle d_{Sm}\rangle/d)\right] \tag{42}$$

The distribution parameter suggests that the dominant factor to determine it would be the void fraction. For extreme cases, such as concentrated void profile and sharp liquid velocity profiles around the tube center, the distribution parameter may exceed 1.2, as reported by Goda et al. (2003) [30].

Secondary flows and vortices occur in the impeller. The phases may behave as co-current or counter-current flow. The operational parameters may influence the flow direction at the impeller inlet, which may lead to increased shock losses. These are things that affect the distribution parameter. Therefore, the value of C_0 found by Eq. 33, equal to 1.23, seems reasonable with the observed ones in turbulent flow in the tubes.

4.2 | Analysis of forces acting on the bubbles

The motion of bubbles in laminar or turbulent flows is much more complex than that of rigid solid particles. The interface between bubbles and liquid is not rigid due to the internal flow inside the bubbles. This condition implies a relative velocity at the surface. Therefore the drag coefficient is reduced compared to solid particles. The drag coefficient C_D is given as a function of the particle Reynolds number Re_P (Ishii and Hibiki, 2010 [24]):

$$Re_P = \frac{\rho_1\, d_b\, |v_1 - v_2|}{\mu_1} = \frac{\rho_1\, d_b\, |v_s|}{\mu_1} \tag{43}$$

The drag coefficient may be altered by numerous physical effects, such as turbulence of the surrounding flow, surface roughness of the particle, particle shape, wall effects, compressibility of the fluids, rarefaction effects and particle concentration effects. All these effects can, in general, only be accounted for by empirical correction factors derived from detailed experiments. The Appendix B in supplementary material has a discussion about the drag for the bubble, which in our case is approximately 0.37 as expected for the bubbles in filtered water.

The bubble' shape has its impact in the drag coefficient. Thus, it was discussed in function of Eötvos number, E_o,

Morton number, M, and Reynolds number, Re. It is possible to observe that not all the bubble are spherical, a portion is wobbling. This discussion was showed in Appendix B.

The coefficient ΔC^{∞} was calculated with the term $A_1^{'}$. This coefficient is studied apart, but it relates Basset and added mass, thus the conclusions presented here consider both terms together.

The added mass coefficient for an individual particle is expected to depend on the void fraction of the surrounding medium. Zuber (1964) [26] first addressed this issue using a cell method and found that the added mass for spherical bubbles increased with the gas volume fraction, α. Odar and Hamilton (1964) [31] proposed the calculation of coefficients for Basset and added mass as functions of the acceleration number, A_c.

$$C_V = 2.1 - \frac{0.132}{A_c^2 + 0.12} \qquad C_B = 0.48 + \frac{0.52}{(A_c + 1)^3} \tag{44}$$

$$\text{where:} \qquad A_c = \frac{|\,\vec{v}_1 - \vec{v}_2\,|^2}{d_B |d\,|\,\vec{v}_1 - \vec{v}_2\,|/d\,t\,|}$$

For low values of A_c, C_V was found to tend towards the value of 1.05 while the value of 0.5 was recovered for a high A_c. However, this value is not so easy to be achieved once other forces are present on bubbles, such as drag, which can affect the calculation if they are not well modeled.

The studies by Michaelides and Roig (2011) [32] showed that the added mass coefficient should be constant, equal to 1, and that the Basset coefficient should be expressed as dependent on the Strouhal number. The analysis showed that the function of the history term is better correlated with the Reynolds and Strouhal numbers rather than the acceleration number that was used originally by Odar and Hamilton (1964) [31]. The Strouhal number describes the behavior of oscillatory flows. In this context the fluid time scale is the reciprocal value of the characteristic fluid oscillations.

$$C_B = 2.0 - 1.0533\left[1 - exp\left(-0.14\,Re_P\,Sr^{0.82}\right)^{2.5}\right] \tag{45}$$

The general expression of Basset force depends on the vorticity diffusion process. The well-known Basset's expression is found in the limit of unsteady Stokes flow for a rigid sphere. In the case of a bubble, while vorticity comes from a no-slip condition at a rigid surface, the bubble tends to vanish the shear stress in its curved surface, and thus vorticity tends to be non-zero. This means that, when a particle experiences a sudden change in velocity, a sheet of infinite vorticity is generated at its surface. This effect is even more complicated for bubbles (Magnaudet, 1997 [33]).

The term ΔC was calculated by the model, considering the void fraction, and it was equal to 1.24. Calculating the same term ΔC using the expression from the literature results in a value of 1.19, which presents a difference of 4%. Again, this term is related to both forces: added mass and Basset.It is in good agreement with the values from the literature, since the sum of their results is near 1. The drift-flux model and the slip model developed by Eqs. 33 and 29, respectively, are in good agreement with literature values, as they are compared with experiments made in tubes.

4.3 | General discussion

In this section, the experimental and modeling results were discussed. The experimental values calculated using the post-processing of images were shown in Table 6. Summarizing some important information:

TABLE 6 Impeller rotation ω, mass gas flow rate $\dot{m}$, pressure increment ΔP, mixture volumetric flux in $\hat{s}$ direction j_{ms}, bubble velocity v_2 and gas void fraction α.

	ω	$\dot{m}$	ΔP	j_{ms}	v_2	α	α_{exp}
	$[rpm]$	$[kg/h]$	$[Pa]$	$[mm/s]$	$[mm/s]$	10^{-3}[-]	10^{-3}[-]
1	600	0.025	1007	922	1159	4	4
2			2280	808	1095	5	6
3			3006	715	1056	5	6
4			3886	603	979	6	7
5	900	0.025	541	1469	1736	3	4
6			4579	1255	1659	4	5
7			7260	1052	1549	4	5
8			9318	857	1433	4	7
9	900	0.012	419	1460	1748	2	2
10			4168	1266	1691	2	2
11			8078	1027	1557	2	3
12			9025	863	1434	2	4
13	1200	0.025	262	1990	2365	2	2
14			5246	1807	2310	2	2
15			11341	1534	2174	2	2
16			16589	1181	1923	3	3

- r_i, r_o, β and h are geometric constants measured from the impeller.
- Q_m, λ and Δp are known from the experiments.
- $\bar{P}$ and $\bar{T}$ are the mean pressure and mean temperature, respectively. With them it is possible to calculate ρ_1, ρ_2, μ_1 and μ_2.
- $\overline{v_{2,s}}$ is measured from the image processing. The in situ velocities of bubbles are an average on the impeller's space in $\hat{s}$ direction.

The experimental data can be compared with the model following the next steps:

1. As demonstrated before, $\overline{j_{ms}}$ is calculated using Eq. 31.
2. α is estimated once $v_{2,s}$ was measured from experimental data ($\alpha = \lambda \overline{j_{ms}} / \overline{v_{2,s}}$).
3. With α acquired, it is possible to calculate: $\{\rho_m, \overline{\rho_m}, \tilde{\rho}_m \, \Delta\rho, \overline{\Delta\rho}, \tilde{\Delta\rho}\}$.

Table 6 shows the mean values for bubbles characteristics in each experiment. Besides, the table presents the

rotational velocity ω, mass gas flow rate $\dot{m}$, pressure increment ΔP, mixture volumetric flux in $\hat{s}$ direction j_{ms}, bubble velocity v_2 and gas void fraction α given by the model and from the experimental data α_{exp}.

The calculated values of void fraction were compared with those given by the image processing technique, showing close values. However, as the number of bubbles increases, the difference between them increases. The swarm effect provoked by this significantly changes the calculus of gas void fraction. Besides, the height of the gas is not known; this is another source of uncertainty in the calculus. The highest condition of the amount of gas inside the impeller happens when the flow pattern is in segregated flow.

5 | CONCLUSIONS

This paper presented an experimental investigation of the two-phase flow, properly water and air, inside an electric submersible pump (ESP) impeller. The air is added at the intake of the pump tube entrance. The visualization prototype was designed by Monte Verde et al. [12], and the same experimental apparatus was used. The air bubbles were filmed with a high-speed camera as they cross the pump's impeller. The velocities and the diameters were computed from acquired images with numerical scripts written in the course of this work.

The instantaneous fields of gas bubbles velocities were obtained by a sequence of scripts, which for example, have the capability to enhance the edge of the bubbles. The post-processing was able to capture the bubble's centroids in the first part of the code. In the second part, the bubble's velocities were calculated. As the impeller rotated, two kinds of velocities were possible to calculate, the radial and circumferential. The velocities were calculated for 600 rpm, 900 rpm and 1200 rpm. When the tests were performed at 1500 rpm, the bubbles were very small, which made their treatment impossible. However, the dimensionless analysis and similarity laws were useful to expand the knowledge obtained by the experimental data collected.

The code developed was verified manually to ensure its functional operation. Its capability to measure a high amount of experimental data allowed the use of statistics for bubble's behavior. The threshold number is an important parameter inside the code that is arbitrarily set by the user.

A drift-flux model for the two-phase gas-liquid flow inside the impeller was developed. The model was based on blade coordinate system, $\hat{s}$ and $\hat{n}$ correlated with azimuth and radius coordinates, $\hat{\theta}$ and $\hat{r}$. The concept of radial cascade was used by Brennen (2011) [23]. The equations of Mass and Momentum were developed and experimental data provided by the post-processing of images was used to validate the model. The viscous stress tensor was modeled through an analogy with the flow inside a rectangular duct. A closure relationship for the momentum transfer was also used.

The proposed friction factor encompasses all losses expected to happen inside the impeller. The closure of the model showed that the proposed friction factor increases with increasing the pump flow rate as expected, as it goes far from the Best Efficiency Point. However, for flow rate points near the Q_{BEP}, the friction factor is comparable to the one proposed by Vieira (2014) [13].

From the drift-flux model, parameters such as C_0 were discussed in section 4.1. Besides, the interphase momentum transfer was analyzed and the forces acting in a bubble were described. The parameters such as drag coefficient, virtual mass and Basset coefficient values showed good agreement with the ones observed in the literature. With these parameters, it was possible to analyze the forces acting on the bubble and propose, based on the literature, transition criteria for surging and gas locking phenomena showing good agreement with the experimental data.

The further improvement of the modeling may lead to better design of geometries for pump impellers under gas-liquid flows conditions, for example.

Acknowledgments

The authors are grateful to ANP (National Agency of Petroleum and Biofuels) for providing financial support for this work through its PRH program and to Petrobras. The authors acknowledge the CNPq (National Council for Scientific and Technological Development, Brazil) for the grant given under Contract Number 310191/2020-3. Acknowledgments are also extended to the School of Mechanical Engineering (FEM), to the University of Campinas (UNICAMP), to the Center for Petroleum Studies (CEPETRO), to the ALFA – Artificial Lift & Flow Assurance Research Group, and to Espaço da Escrita – Pró-Reitoria de Pesquisa, UNICAMP - for the language services provided.

REFERENCES

1. Feng J, Benra FK, Dohmen H. Application of different turbulence models in unsteady flow simulations of a radial diffuser pump. *Forschung im Ingenieurwesen*. 2010;74(3):123–133.

2. Mikielewicz J, Wilson DG, Chan TC, Goldfinch AL. A method for correlating the characteristics of centrifugal pumps in two-phase flow. *Journal of fluids Engineering*. 1978;100(4):395–409.

3. Wilson DG, Chan T, Manzano-Ruiz J. Analytical models and experimental studies of centrifugal-pump performance in two-phase flow.[PWR]. tech. rep.Massachusetts Inst. of Tech., Cambridge (USA). Dept. of Mechanical Engineering 1979.

4. Estevam V. *Uma analise fenomenologica da operação de bomba centrifuga com escoamento bifasico*. PhD thesisPh. D. thesis, Universidade Estadual de Campinas 2002.

5. Barrios LJ. *Visualization and modeling of multiphase performance inside an electrical submersible pump*. PhD thesisUniversity of Tulsa 2007.

6. Solano EA. *Viscous effects on the performance of electro submersible pumps (ESP's)*. PhD thesisUniversity of Tulsa 2009.

7. Paternost G. Estudo experimental sobre bomba centrífuga operando com fluido viscoso e escoamento bifásico gás-líquido. Master's thesisUniversity of Campinas 2013.

8. Biazussi J. *Modelo de deslizamento para escoamento gás-lıquido em bomba centrıfuga submersa operando com lıquido de baixa viscosidade*. PhD thesisPh. D. thesis, Universidade Estadual de Campinas 2014.

9. Murakami M, Minemura K. Effects of entrained air on the performance of a centrifugal pump: 1st report, performance and flow conditions. *Bulletin of JSME*. 1974;17(110):1047–1055.

10. Murakami M, Minemura K. Effects of entrained air on the performance of a centrifugal pump: 2nd report, effects of number of blades. *Bulletin of JSME*. 1974;17(110):1286–1295.

11. Gamboa J. *Prediction of the transition in two-phase performance of an electrical submersible pump*. PhD thesisUniversity of TulsaOK, USA 2009.

12. Verde WM, Biazussi JL, Sassim NA, Bannwart AC. Experimental study of gas-liquid two-phase flow patterns within centrifugal pumps impellers. *Experimental Thermal and Fluid Science*. 2017;85:37–51.

13. Vieira TS. Análise das Perdas de Carga no Escoamento Monofásico em Rotor De Bomba Centrífuga Submersa Utilizada na Elevação de Petróleo. Master's thesisUniversidade Estadua do Norte Fluminense Darcy RibeiroMacaé/RJ 2014.

14. Shoham O. *Mechanistic Modeling of Gas/liquid Two-phase Flow in Pipes*. Spe 2005.

15. Cubas JM, others . Estudo experimental do escoamento bifásico ar-água em uma bomba centrífuga radial. Master's thesisUniversidade Tecnológica Federal do Paraná 2017.

16. Stel H, Ofuchi EM, Sabino RH, *et al.* Investigation of the motion of bubbles in a centrifugal pump impeller. *Journal of Fluids Engineering.* 2019;141(3).

17. Penteado MRM, Franklin EDM. Velocity fields of a bed-load layer under a turbulent liquid flow. *Experimental Thermal and Fluid Science.* 2016;78:220–228.

18. Monte Verde W. *Bombas Centrífugas Submersas: Visualização do escoamento bifásico gás-líquido, operação com fluido viscoso e modelagem de desempenho*. PhD thesisUniversidade Estadual de Campinas, UNICAMPCampinas 2016.

19. Oppenheim AV, Schafer RW. *Discrete-time signal processing*. Pearson Education 2014.

20. Gonzalez RC, Woods RE. *Digital Image Processing*. Prentice-Hall, Inc 2008.

21. Sonka M, Hlavac V, Boyle R. *Image processing, analysis, and machine vision*. Cengage Learning 2014.

22. Hinkelmann K, Kempthorne O. *Design and analysis of experiments: advanced experimental design*;2. Wiley Online Library 2005.

23. Brennen CE. *Hydrodynamics of pumps*. Cambridge University Press 2011.

24. Ishii M, Hibiki T. *Thermo-fluid dynamics of two-phase flow*. Springer Science & Business Media 2010.

25. Churchill SW. Friction-factor equation spans all fluid-flow regimes.. *Inist-CNRS.* 1977.

26. Zuber N. On the dispersed two-phase flow in the laminar flow regime. *Chemical Engineering Science.* 1964;19(11):897–917.

27. Wallis GB. *One-dimensional two-phase flow*. McGraw-Hill 1969.

28. Clark N, Flemmer R. Predicting the holdup in two-phase bubble upflow and downflow using the Zuber and Findlay drift-flux model. *AIChE journal.* 1985;31(3):500–503.

29. Hibiki T, Ishii M. Distribution parameter and drift velocity of drift-flux model in bubbly flow. *International Journal of Heat and Mass Transfer.* 2002;45(4):707–721.

30. Goda H, Hibiki T, Kim S, Ishii M, Uhle J. Drift-flux model for downward two-phase flow. *International journal of heat and mass transfer.* 2003;46(25):4835–4844.

31. Odar F, Hamilton WS. Forces on a sphere accelerating in a viscous fluid. *Journal of Fluid Mechanics.* 1964;18(2):302–314.

32. Michaelides EE, Roig A. A reinterpretation of the Odar and Hamilton data on the unsteady equation of motion of particles. *AIChE Journal.* 2011;57(11):2997–3002.

33. Magnaudet JJ. The forces acting on bubbles and rigid particles. in *ASME Fluids Engineering Division Summer Meeting, FEDSM*;97:22–26 1997.

34. Shah R. A correlation for laminar hydrodynamic entry length solutions for circular and noncircular ducts. *J. Fluids Eng.*. 1978.

35. Sun D, Prado MG, others . Single-phase model for electric submersible pump (ESP) head performance. *SPE Journal.* 2006;11(01):80–88.

36. Amaral GDL. *Modelagem do escoamento monofásico em bomba centrífuga submersa operando com fluidos viscosos*. PhD thesisPh. D. thesis, Universidade Tecnologica Federa do Parana 2007.

37. Haberman WL, Morton R. An experimental investigation of the drag and shape of air bubbles rising in various liquids. tech. rep.David Taylor Model Basin Washington DC 1953.

38. Clift R, Grace JR, Weber ME. *Bubbles, drops, and particles*. Courier Corporation 2005.

39. Hibbeler RC. *Engineering Mechanics: Dynamics*. Prentice Hall 2010.